Open Research Online

The Open University's repository of research publications
and other research outputs

Shallow structure beneath the Central Volcanic Complex of Tenerife from new gravity data: implications for its evolution and recent reactivation

Journal Item

How to cite:

Gottsmann, J.; Camacho, A. G.; Marti, J.; Wooller, L.; Fernandez, J.; Garcia, A. and Rymer, H. (2008). Shallow structure beneath the Central Volcanic Complex of Tenerife from new gravity data: implications for its evolution and recent reactivation. Physics of the Earth and Planetary Interiors, 168(3-4) pp. 212–230.

For guidance on citations see FAQs.

© 2008 Elsevier B.V.

Version: Accepted Manuscript

Link(s) to article on publisher's website:
http://dx.doi.org/doi:10.1016/j.pepi.2008.06.020

Copyright and Moral Rights for the articles on this site are retained by the individual authors and/or other copyright owners. For more information on Open Research Online's data policy on reuse of materials please consult the policies page.

oro.open.ac.uk

* Manuscript
Click here to view linked References

Shallow structure beneath the Central Volcanic Complex of Tenerife from new gravity data: Implications for its evolution and recent reactivation

J. Gottsmann[1], A.G. Camacho[2], J. Martí[3], L. Wooller[4], J. Fernández[2], A. García[5], H. Rymer[4]

[1] Department of Earth Sciences, University of Bristol, Wills Memorial Building, Queens Road, Bristol BS8 1RJ, United Kingdom

[2] Instituto de Astronomia y Geodesia (CSIC-UCM), Ciudad Universitaria, Pza. de Ciencias, 3, 28040 Madrid, Spain

[3] Institute of Earth Sciences "Jaume Almera", CSIC, Lluís Solé Sabarís s/n, Barcelona 08028, Spain

[4] Department of Earth and Environmental Sciences, The Open University, Walton Hall, Milton Keynes, MK7 6AA, United Kingdom

[5]Department of Volcanology, Museo Nacional de Ciencias Naturales, CSIC, C/ José Gutiérrez Abascal, 2, 28006 Madrid, Spain

Abstract

We present a new local Bouguer anomaly map of the Central Volcanic Complex (CVC) of Tenerife, Spain, constructed from the amalgamation of 323 new high precision gravity measurements with existing gravity data from 361 observations. The new anomaly map images the high-density core of the CVC and the pronounced gravity low centred in the Las Cañadas caldera in greater detail than previously available. Mathematical construction of a subsurface model from the local anomaly data, employing a 3-D inversion based on "growing" the subsurface density distribution via the aggregation of cells, enables mapping of the shallow structure beneath the complex, giving unprecedented insights into the sub-surface architecture. We find the resultant density distribution in agreement with geological and other geophysical data. The modelled subsurface structure supports a vertical collapse origin of the caldera, and maps the headwall of the ca. 180ka Icod landslide, which appears to lie buried beneath the Pico Viejo – Pico Teide stratovolcanic complex. The results allow us to put into context the recorded ground deformation and gravity changes at the CVC during its reactivation in spring 2004 in relation to its dominant structural building blocks. For example, the areas undergoing the most significant changes at depth in recent years are underlain by low-density material and are aligned along long-standing structural entities, which have shaped this volcanic ocean island over the past few million years.

1. Introduction

The Central Volcanic Complex (CVC) of Tenerife (Canary Islands, Spain)), which includes the 16 x 9 km wide Las Cañadas caldera (LCC, Figure 1), reactivated after an almost century-long period of quiescence in spring 2004, with increased seismicity (including felt earthquakes) and subsurface mass addition into its north-western and western portions (García et al., 2006; Tárraga et al., 2006; Gottsmann et al., 2006; Almendros et al., 2007). It has been speculated that earthquake locations and density changes during the reactivation may be controlled by the internal structure of the CVC (Martí et al., 2008a). However, the available geophysical information on its sub-surface architecture is mainly based on rather crude surveys highlighting large wavelength anomalies such as from aero-magnetic data (Araña et al., 2000; García et al., 2007) or gravimetric data with substantial uncertainties (Araña et al., 2000). A detailed assessment of structural controls on the spatio-temporal variations in geophysical parameters during the recent reactivation thus remains ambiguous. At other collapse calderas (e.g. Long Valley, Valles, Toba, Campi Flegrei) geophysical imaging has provided important insights into their internal architecture including the identification of potential magma and hydrothermal reservoirs (e.g. Sanders et al., 1995; Aprea et al., 2002 Guidarelli et al., 2002; Masturyono et al., 2001). Such reservoirs may play an important role during post-collapse processes, including episodes of unrest (see Martí et al., 2008b for a recent review). In light of the recent unrest, knowledge about the shallow subsurface beneath the CVC is of great importance, and provided the motivation for this study. This work also aims to contribute to the discussion as to the origin of the Las Cañadas Caldera (LCC): lateral

collapse due to edifice instability (Cantagrel et al., 1999) or vertical collapse due to explosive volcanism (Martí and Gudmundsson, 2000) having been proposed.

We present results from a new series of gravity measurements performed at the CVC over the past few years, which, combined with existing gravimetric data, enable us to image its shallow sub-surface density distribution at a higher resolution than previously possible.

2. Previous geophysical work

While the surface geology of the CVC (Fig. 1) has been a target in the past (e.g. Martí et al., 1994; Ablay et al., 1998; Ablay and Martí, 2000), the complex's internal structure remains rather enigmatic. Previous geophysical studies have focused on obtaining sub-surface images based on large wavelength (>> 1 km) anomalies (MacFarlane and Ridley, 1968; Ablay and Kearey, 2000; Watts et al., 1997; Araña et al., 2000) but have not provided information on the shallow structure beneath the CVC, including the caldera itself. Ablay and Kearey (2000), provided a coherent interpretation of the magmatic and structural evolution of Tenerife from gravity data predominantly collected in the 1980s and 90s by members of the Instituto de Astronomia (CSIC-UCM) and the Instituto Geografico Nacional (Camacho et al., 1991; Araña et al., 2000). Ablay and Kearey's emphasis lay in the integration of a rich petrological data set with the existing gravimetric data. The original gravity data suffered from significant uncertainties stemming from both terrain correction methods and control of benchmark elevation using topographic maps and barometers, which resulted in uncertainties in the Bouguer anomalies on the order of 5 mGal (1 mGal=10^{-5}m/s^{-2}) (Ablay and Kearey, 2000). One of the first high-resolution geophysical images to a depth of approximately 1500 m beneath the LCC floor was

provided by the audiomagnetotelluric study of Coppo et al. (2008), which enabled the identification of three adjacent bowl-shaped depressions consistent with a multiple-event vertical collapse origin of the LCC.

3. Geological background

The geological and tectonic evolution of the triangular island of Tenerife and the CVC was described in recent papers (Martí et al., 1994; Martí et al., 1998; Araña et al., 2000) and we therefore only provide a short summary. The Canary Islands form a volcanic archipelago with a long-standing history of volcanic activity that began more than 40 million years ago (Araña and Ortíz, 1991). More than a dozen eruptions have occurred on the islands of Tenerife, Lanzarote, and La Palma since the 16^{th} century. Tenerife, the largest of the Canary Islands, has an eruptive history of over 12 million years, including a shield building phase and the construction of a central volcanic structure, the Las Cañadas edifice (LCE) from 3.5 Ma onwards (Martí et al., 1994). Table 1 provides a stratigraphic scheme of the island, and highlights the main constructive and destructive episodes during its formation. The LCE is composed of a mafic post-shield Lower Group (>3.5 Ma – 1.57 Ma), overlain by the Upper Group comprising three felsic formations (1.57 Ma -0.179 Ma).

The evolution of the LCE comprises both constructive and destructive phases, including vertical and lateral collapses with volumes on the orders of several to tens of km^3 (Martí et al., 1997). Martí et al. (1994) propose at least three vertical collapses during Upper Group times, which resulted in the formation of the LCC (Table 1). High walls nowadays bound the LCC to the southwest, south, east and northeast.

Over the past 170-190 ka, the prominent Pico Viejo - Pico Teide (PV—PT) volcanic complex was emplaced inside the caldera depression during predominantly effusive but also explosive activity (Ablay and Martí, 2000; Edgar et al., 2007). The PV-PT complex appears to be fed by both shallow-level (< 5 km) phonolitic magma reservoirs and deeper-seated basaltic magma patches (Ablay and Hürlimann, 2000; Ablay and Martí, 2000). Recent (< 2 ka) volcanic activity was located both on the PV—PT complex (explosive and effusive phonolitic eruptions) and along two extensional structural lineaments referred to as the NW—SE oriented Santiago Rift, and the SW-NE striking Dorsal Ridge (both rifts are dominated by monogenetic mafic eruptions). Historic eruptions at these centres were fed by mafic magmas and occurred in 1704, 1706, 1798, and 1909. To the north of the CVC lie the valleys of Icod and Orotava, which are interpreted to represent scars from large lateral collapses (landslides). The absence of a visible caldera wall to the North has led some workers to infer a lateral collapse origin of the LCC (Cantagrel et al., 1999; Ancochea et al., 1999). Others see clear evidence for vertical collapse origin of the LCC based on the abundance and nature of pyroclastic deposits consistent with explosive caldera formation (Martí et al., 1998; Bryan et al., 1998; Ablay and Hürlimann, 2000; Martí and Gudmundsson, 2000; Brown and Branney, 2004).

4. Gravity data

a) New gravity survey

All 323 new gravity measurements were performed by the same operator (JG) at the CVC between May 2004 and November 2006 using LaCoste&Romberg gravimeter G-403 (Fig. 1). The accuracy of individual readings was maintained

144 through regular reoccupation of each station and the reference station. The reference
145 was conveniently located in the caldera depression at 340088.27m Easting and
146 3124255.73m Northing, at an ellipsoidal elevation of 2223.83 m. The reference was
147 occupied between 4 and 8 times per day depending on the design of measurement
148 loops to check for instrument drift and tares. At each benchmark the reading was
149 derived by the averaging of between 5-10 manual readings taken over a few minutes,
150 depending on benchmark stability and ambient noise. The error on the raw readings is
151 less than 0.02 mGal. Location and elevation data were provided by differential GPS
152 measurements (operated by LW), conducted at the same time as the gravity
153 measurements. Leica System 530 receivers and AT502 antennas were used, with data
154 sampling at 1 Hz. A reference station was established (with matching occupation
155 frequency of 1 Hz running for a total of more than 250 hrs), for which absolute
156 WGS84 co-ordinates were derived. A rover GPS receiver, mounted on a 1.9 m-high
157 staff, was placed at the measurement point and recorded for periods of between 60
158 and 180 seconds, depending upon satellite visibility and the distance to the reference.
159 Post-processing of the GPS data was carried out using Leica Geosystems' Ski-Pro
160 software. 2σ errors for most positions were generally under 5 cm in the Z axis and
161 better than 4 cm in the X and Y axes. Fig. 2 shows the location of the new
162 gravity/GPS benchmarks which provide coverage of the LCC, the PV-PT complex
163 and the Santiago Rift. An additional 361 gravity data (from a total set of 975 covering
164 the entire island) obtained earlier are used for investigating the wider area surrounding
165 the CVC (Camacho et al., 1991, Araña et al., 2000). These earlier gravity readings
166 are reported with an uncertainty of 1.2 mGal. The significantly larger error in the
167 earlier gravity data compared to the new data is due to uncertainties in benchmark
168 elevation.

169

170 ## b. Terrain density

171 The terrain density is among the most critical parameters for gravimetric data
172 reduction and choosing the 'right', i.e., realistic, terrain density for a whole island
173 (with bimodal magmatism/volcanism spanning several million years and the
174 associated variety in eruptive products) is prone to errors. Terrain effects are
175 significant on Tenerife as the CVC represents the top of a volcanic edifice rising to
176 more than 3.7 km elevation within 12 km from the northern shoreline, and extending
177 more than 3.5 km below sea level. Despite these complexities, it is possible to deduce
178 an optimal value for terrain density from both gravity and elevation data. According
179 to a general assumption (Nettleton, 1939), a suitable density value must produce a
180 minimum correlation between gravity anomaly (***Δg***) and elevation (***h***). However, this
181 approach can lead to erroneous density estimates, for example if long wavelength
182 components of both gravity and topography are correlated due to deep structural
183 features. The general terrain on Tenerife follows a convex geometry common to all
184 volcanic islands related to the intrusive and extrusive nature of ocean island building,
185 and thus the gravity anomaly will also follow this pattern. A more realistic value for
186 the terrain density can be obtained by looking for the minimum correlation between
187 the shortest wavelength components of both gravity and topography.
188 For each benchmark P_i, we therefore calculate the short wavelength values $\Delta\widetilde{g}_i$ and
189 $\Delta\widetilde{h}_i$ for the gravity anomaly and elevation, respectively, by removing regional values
190 determined as mean values between P_i and surrounding benchmarks P_j up to a radius
191 r:
192

$$\Delta\tilde{g}_i = \Delta g_i - \frac{1}{n_i}\sum_J \Delta g_j \,, \qquad \Delta\tilde{h}_i = \Delta h_i - \frac{1}{n_i}\sum_J \Delta h_j$$

where distance (Pi, Pj) ≤ r.

The optimal theoretical terrain density ρ_t corresponds to the minimum correlation between the resulting $\Delta\tilde{g}_i$ and $\Delta\tilde{h}_i$ values. Fig. 3 gives terrain densities (kg/m^3) as a function of *r*. However, we choose a terrain density accounting for both theoretical constraints and measured densities of exposed lithologies of the CVC. Ablay and Kearey (2000) report more than 30 measured bulk densities of Tenerife rock types. Calculating the mean values for their reported rock types (except for Teno and Dorsal ridge basalts) and weighting the occurrence of effusive and flow deposits against fall deposits (0.8 vs. 0.2, respectively), to account for exposed CVC lithologies (Table 2), we derive 2200±271 kg/m^3. The mean value is consistent with our theoretical minimum correlation for r of about 3 km, providing a reasonable wavelength for topographic and gravity anomalies. We thus use a terrain density of 2200 kg/m^3 for our gravity reduction.

c) Gravity data reduction

Standard techniques for gravimetric data reduction for the effect of Earth and ocean tides, latitude and benchmark elevation were employed. Ocean loading effects were corrected using the Schwiderski global ocean tide model (Schwiderski, 1980). Continuous gravity observation, performed by an automated Burris gravity meter (B-28) in 2007 over a period of 8 days in the Las Cañadas caldera, revealed that residual ocean loading effects amount to less than 0.01 mGal and are thus negligible for our purpose.

The earlier gravity data were referenced to the absolute gravity reference IGSN71 (Morelli et al., 1974). In order to merge the data sets, we determined two sets of Bouguer anomalies, one using solely the new data and the second using only the earlier data. We then deduced an offset value, which produced a maximum autocorrelation between the two sets of anomaly data. This gravity offset was then used to combine the two data sets to form a single coherent set of gravity data. This technique involving global overlapping of individual data is superior to techniques based on matching few common benchmarks to calculate an offset value, as local inaccuracies could be propagated, resulting in an erroneous final data set.

Free-air and Bouguer corrections, respectively, were performed with respect to theoretical predictions based on GRS80 [Geodetic Reference System 1980] using a standard free-air gradient of -0.308 mGal/m and the above derived terrain density of 2200 kg/m^3 for the Bouguer correction

d) Terrain correction

To correct for the topographic effects (on-shore Tenerife, neighboring islands and off-shore areas) on gravity measurements, we employed an automated algorithm based on dense circular zones (34 zones from 1 m to 100 km radius, 894 compartments in total), similar to Hammer zones, around the individual benchmarks (Hammer, 1939). A 10 m digital elevation model (DEM), constructed from topographic maps provided by the Instituto Geografico Nacional (IGN), approximated the immediate on-shore topography up to 895 m distance from each gravity point. For on-shore distances greater than 895 m, we used a 100 m DEM. For the surrounding marine areas, satellite altimetry data (http://topex.ucsd.edu/cgi-bin/get_data.cgi and

243 local charts were used to provide information about the local geoid and bathymetry
244 (Smith and Sandwell, 1997). Similar to the Hammer reduction procedure, average
245 elevations were calculated for each compartment and the terrain effect in each
246 compartment was propagated to obtain the final terrain correction value for each
247 benchmark.

248 The so derived terrain corrections for the gravity benchmarks vary between 8.8
249 mGal and 97.7 mGal, with an average of 19.3 mGal. The maximum correction applies
250 to a benchmark at the base of Teide's summit cone. Possible errors in the choice of
251 the terrain density ρ_t are accounted for in the modelling process. For this, an
252 additional unknown $\delta\rho_t$, which represents a correction to the initially assumed terrain
253 density, is included in the inversion routine as described below.

254

255 ## e) Regional gravity trend

256 A very long-wavelength component of gravity variations can be produced by
257 crustal structures defining a regional trend in the resultant gravity data. This effect
258 needs to be accounted for in creating a local Bouguer anomaly map of the CVC. We
259 used Geosat and ERS 1 satellite altimetry and gravity data (http://topex.ucsd.edu/cgi-
260 bin/get_data.cgi; (Sandwell and Smith, 1997)) to quantify the regional gravity trend
261 considering an area up to a distance of 100 km around Tenerife and 3 km radial
262 spacing between individual nodes.

263 Using the free-air satellite anomaly data combined with bathymetry and geoid
264 heights, we determined the regional Bouguer anomaly taking 2900 kg/m^3 as the mean
265 background density for oceanic crust (Carlson and Raskin, 1984). We determined a
266 smoothed linear trend of 0.27±0.03 mGal/km with azimuth N113ºE, which represents
267 the very long wavelength component superimposed on the local anomaly. It is in

reasonable agreement with a general average value of 0.2 mGal/km obtained by Bosshard and MacFarlane (1970) extending from west of La Palma and El Hierro to Gran Canaria. This trend is believed to be due to crustal thickening towards the African continent.

Subtracting the regional trend from the data, we obtain the local Bouguer anomaly (Fig. 4), which highlights local sub-surface structures. These Bouguer anomaly data are then employed for the mathematical inversion.

5. Gravity inversion

a. Theory and sensitivity

The inverse gravimetric problem, namely the determination of a sub-surface density distribution consistent with an observed gravity anomaly, has an intrinsically non-unique solution (e.g. Al-Chalabi, 1971). Moreover, the available data are always insufficient and inaccurate to resolve ambiguities. One can, however, obtain realistic solutions by including additional constraints on model parameters (subsurface structure) and data parameters (statistical properties of inaccurate data, e.g. Gaussian distribution). The non-linear inversion methods that delineate the geometrical properties of anomalous bodies with prescribed density contrasts (e.g. Pedersen, 1979; Barbosa et al., 1997) are of course limited by the underlying hypothesis on source density. However, these techniques provide results worth exploring. For full non-linear treatments, methods based on the exploration of model possibilities often give the best results (Tarantola, 1988). This exploration process can for example be conducted randomly (Silva and Hohmann, 1983).

292 In this study we use the inversion routine presented in Camacho et al. (2000 and
293 2002), which has also been applied in other gravimetric studies (Camacho et al., 2001,
294 2007). The inversion process constructs a subsurface model defined by a 3-D
295 aggregation of *M* parallelepiped cells, which are filled, in a "growth" process, by means
296 of prescribed positive and/or negative density contrasts. The design equation to relate
297 observables, i.e., the gravity anomaly Δg_i at *N* benchmarks *(x_i,y_i,z_i),* with modelling
298 parameters, and residuals v_i is:

299 $$\Delta g_i = \sum_{j \in J^+} A_{ij} \Delta \rho_j^+ + \sum_{j \in J^-} A_{ij} \Delta \rho_j^- + \delta g_{reg} + \delta g_{top} + v_i \quad , \quad i = 1,...,N \quad ,$$

300 (1)

301 where A_{ij} is the vertical attraction for unit density for the *j*-th parallelepiped cell upon
302 the *i*-th observation point, $\Delta \rho_j^-$, $\Delta \rho_j^+$ are prescribed density contrasts (negative and
303 positive) for the *j*-th cell, J^+, J^- are sets of indexes corresponding to the cells filled
304 with positive or negative density values, and δg_{reg}, δg_{top} are optional terms for
305 regional trend and additional topographical correction given by

306 $$\delta g_{reg} = p_0 + p_x (x_i - x_M) + p_y (y_i - y_M) \quad , \quad i = 1,...,N \quad , \qquad (2)$$

307 $$\delta g_{top} = \delta \rho_T \; C_i \, . \qquad (3)$$

308 Here p_0, p_x, p_y are parameters for the linear trend, x_M, y_M are averaged coordinates, C_i
309 are coefficients for the terrain correction and $\delta \rho_T$ is an optional additional value with
310 respect to the initially adopted terrain density. In Eqns. 1-3, J^+, J^- (cells filled with
311 positive and negative density contrast), p_0, p_x, p_y, and $\delta \rho_T$ (regional parameters) are
312 the main unknowns to be determined by the inversion.

313 The problem of non-uniqueness is usually approached by numerical
314 techniques in the form of a generalised matrix inversion including some form of

315 "perturbation" scheme such as the Levenberg-Marquardt method (e.g. Enmark, 1981;
316 García-Abdeslem, 2000; Marinara and Hall, 2001). In short, the "perturbation" idea of
317 the Levenberg-Marquardt method (and other similar methods) is a numerical
318 approach that involves modification of the usual least square solution for the case of
319 singularity or non-uniqueness, by an "ad-hoc" term or perturbation ($\lambda \boldsymbol{I}$; where $\boldsymbol{I}$ is an
320 identity matrix), which may transform a singularity into non-singularity. Such
321 solutions aim at minimising an objective function that is a combination of the l_2-norm
322 of the residuals ("least squares fit") and the l_2-norm of the model parameters, using a
323 positive value of λ for balance (the so-called damping factor or Lagrange multiplier).
324 The methodology followed in our study can be considered as a generalisation of this
325 numerical approach as outlined by Tarantola (1988). This author gives a general
326 treatment of least-squares inversion methods by including them into a general theory,
327 which represents the inversion problem as a problem of combination of inaccurate
328 information. For instance, the least-squares inversion approach is presented as the
329 combination of observable data with Gaussian uncertainties (given by a covariance
330 matrix $\boldsymbol{Q_D}$) and information on the model, given by a previous model $\boldsymbol{m_{prev}}$ which is
331 also subject to Gaussian uncertainties (given by a covariance matrix $\boldsymbol{Q_M}$). For the
332 case where the previous model is exactly zero ($\boldsymbol{m_{prev}} \equiv \boldsymbol{0}$, no particular previous
333 information on the model is available) the formulae of the general methodology of
334 Tarantola are close to the numerical methods pointed out before. For the particular
335 case of gravity inversions aiming at deriving a unique model of density distribution at
336 depth, the general condition of l_2-minimisation of the model parameters becomes a
337 minimisation condition for the total anomalous mass; i.e. a model involving
338 anomalous bodies with simple and smoothed geometries *and* a minimum total mass is
339 uniquely determined. Accordingly, in order to get unique results from our data

inversion, we adopt a mixed minimisation condition, based on model "fitness" (least square fitness) and "smoothness" (total anomalous mass) (see also Camacho et al., 2002):

$$\mathbf{v}^T \mathbf{Q}_\mathbf{D}^{-1} \mathbf{v} + \lambda \ \mathbf{m}^T \mathbf{Q}_\mathbf{M}^{-1} \mathbf{m} = \min, \tag{4}$$

where $\boldsymbol{m} = \left(\Delta\rho_{1}, ..., \Delta\rho_{M}\right)^T$ (superscript T denotes transpose of a matrix) are density contrast values for the M cells of the model, $\boldsymbol{v} = \left(v_1, ..., v_N\right)^T$ are residual values for the N data points, $\boldsymbol{Q_D}$ is an apriori covariance matrix for uncertainties of the gravity data, $\boldsymbol{Q_M}$ is an apriori covariance matrix for uncertainties of the model parameters, and λ is a factor for selected balance fitness/smoothness of the model. For practical applications λ is selected to produce uncorrelated inversion residuals. In traditional numerical inversion methods based on the Levenberg-Marquardt smoothing approach, an identity matrix $\boldsymbol{I}$ is used in place of $\boldsymbol{Q_M}$. However, taking into account that the cells of the model have different sensitivities (lower for deep or peripheral cells; see below), using a covariance matrix to quantify cell sensitivity based on its geometry and location, will produce more balanced and coherent minimization conditions for the model parameters, and will thus produce more consistent solutions.

In interpreting the inversion results a few important points need to be considered. Although the inversion routine counteracts the problem of non-uniqueness of results via the mixed minimum condition as explained above, there is still some degree of ambiguity in the results. Despite the complexity of the inversion, the resultant models should not be regarded as an exact replication of the sub-surface architecture, as both data collection and post-processing suffer from inaccuracies and assumptions. The modelled density contrasts should be seen as mean values for a particular spatial distribution of cells in the form of a smoothed model. The sensitivity

364 to the data is dependent on the position of each cell within each the model. The
365 sensitivity of very shallow, very deep and very peripheral cells is lower than those
366 located beneath the survey area at depths of about 2 km below the surface. During
367 inversion the size of the cells is variable to account for differences in sensitivity: very
368 deep cells or very peripheral cells are larger then those cells located at shallow depth.
369 Figure 5 shows results from a sensitivity test of the inversion for the particular case of
370 the Tenerife study. We simulate an S-shaped anomalous body with a prescribed
371 density contrast of 800 kg/m^3 located beneath the CVC. Using the same gravity
372 benchmarks employed for the inversion as described in the next section, we calculate
373 the resultant gravity value at each benchmark and then use these data for inversion.
374 The inversion model gives an adequate representation of the simulated body in terms
375 of its geometry. Distortions in the shape of the modelled body with respect to the
376 simulated body are apparent for greater depths as well as in areas of insufficient
377 gravity data. The density contrast is found to be ca. 400 kg/m^3 (i.e., 50% of the
378 prescribed contrast), which represents the value consistent with the minimum total
379 anomalous mass necessary to match the observed Bouguer anomaly (see previous
380 section on inversion theory). In general, while the shape and distribution of the
381 modelled anomalous bodies are indicative of their real features as shown by the above
382 sensitivity analysis and also by the examples given by Camacho et al. (2002), due to
383 the tendency of the methodology to produce models involving a minimum total
384 anomalous mass, the density contrasts are likely to be stronger in reality. It is
385 therefore impossible to attribute a finite "real" value to any density contrast.
386

387 ## b. Inversion of data
388

389 The operational method for solving the design system is a controlled 3-D
390 growth of anomalous bodies by means of an exploratory approach, subject to the fit
391 and smoothness conditions explained in the previous section.

392 From the full data set of 361 existing and 323 new gravity measurements we
393 selected 392 data (Figs. 1 and 2) matching the following conditions: (i) a minimum
394 distance between neighbouring benchmarks of equal or larger than 200 m for the new
395 data (core of the data set) and (ii) equal or larger than 1000 m for the earlier data to
396 account for gravimetric data obtained at the periphery of and outside the CVC.
397 Outliers in the older gravity data were removed. The Bouguer anomaly value Δg_i at
398 each benchmark (i= 1, 2, 3…, 392) and its coordinates were fed into the automated
399 inversion. In a first step, the sub-surface volume was partitioned into 16850
400 parallelepiped cells. The cells had sides ranging from 330 m in the shallowest zone (3
401 km a.s.l.) to 2023 m at a depth of 24 km b.s.l., with an average side of 700 m. Matrix
402 $\boldsymbol{Q_D}$ for the *a priori* covariance of gravity data was considered to be a diagonal matrix
403 corresponding to an assumed standard deviation of ±0.4 mGal for the new data and
404 ±1.2 mGal for the earlier gravity data. Matrix $\boldsymbol{Q_M}$ for *a priori* covariance of the cell
405 distribution geometry was taken as a diagonal normalizing matrix of non-zero elements
406 that matched the diagonal elements of $\boldsymbol{A}^T\boldsymbol{Q_D}^{-1}\boldsymbol{A}$, where $\boldsymbol{A}$ is the design matrix with
407 elements A_{ij}. In a second step, we fitted a rough model based on prescribed (positive and
408 negative) density values in the range between -250 kg/m^3 and 230 kg/m^3. Including the
409 smoothing effect, the resultant anomalous density values for the model are -209 kg/m^3
410 and 184 kg/m^3. The value λ is automatically determined by assuming the condition of
411 zero autocovariance for the final residuals.

412 The former model is obtained without any particular assumption towards the
413 physical properties of the surrounding non-anomalous medium. The anomalous

densities need to be added to some non-anomalous medium density to give the final finite subsurface density distribution. Assuming a homogeneous non-anomalous medium, the final model will be similar to the adjusted model. However, the bimodal evolution of Tenerife, with a basic oceanic shield-building phase succeeded by an evolved stratovolcano building phase warrants the assumption of a significant density contrast between shallower and deeper portions of the island and the crust. As a consequence, large positive density contrasts (>250 kg/m^3) at greater depth, may not be anomalous but rather reflect vertical and horizontal discontinuities with strong density contrasts with respect to shallower depths. A way to accommodate density stratification with increasing depth is to assume a stratified background medium during inversion. In doing so, we followed the hypothesis of a general background stratification, defined by a continuous exponential law for density increase with respect to depth z: $\Delta\rho = \rho_0 + a \exp(-b\ z)$, where ρ_0 is 2200 kg/m^3, a is 580 kg/m^3 and b is 54x10^{-6} m^{-1}. Values for a and b where calculated such as to avoid background density inversion; i.e., high density material overlying low density material in the model. We chose an exponential density increase rather than a linear increase to account for the fact that most of the interior of Tenerife is composed of mafic volcanics, while evolved (phonolitic) material was only erupted with the construction of both the Las Canadas edifice from 3.5 Ma onwards and the PV-PT complex (from 179 ka onwards). We estimate a minimum volume of Tenerife of 15000 km^3, with most of this volume associated with the mafic shield-building phase (ca. 90%). The remaining 10 % of volume includes the Las Cañadas edifice and the PV-PT complex. The maximum estimate for the volume of phonolitic material recognisable at the surface is 250-300 km^3, which mostly corresponds to the Las Cañadas phonolites. We

438 thus assume a maximum proportion of 2% of evolved (phonolitic) as opposed to 98%
439 of mafic material.

440 To produce quasi-homogeneous anomalous structures, we applied the same
441 inversion process as explained above, but account for an anomalous positive density
442 contrast decrease as a function of z: $\Delta\rho = \rho_0 - a\ exp(-b\ z)$. The adjusted inversion
443 model has a "bell" shape with anomalous positive density decreasing, while the
444 background medium shows an exponentially increasing density with depth, and the
445 addition of both results in quasi-homogeneous structures embedded in a stratified
446 medium.

447 While we discuss results from both homogenous and stratified background
448 models, we choose to restrict our interpretations of the inversion results to those
449 obtained from models based on a density-stratification of the background medium.
450 We feel that, despite our simplified stratification, these models provide a more
451 realistic account of the "real" density distribution beneath the CVC at greater depth
452 compared to a homogeneous medium. The modelled shallow structures to depths of
453 about 1000 m bsl differ insignificantly in either model, providing a sound basis for the
454 interpretation of the immediate sub-surface, while accounting for stratification may
455 more realistically image density variations at greater depth. A general value of 41
456 kg/m^3 can be assumed as the mean sensitivity of the cells in either model.
457

458 # 6. Results
459

460 ## a. Bouguer and local anomaly
461

462 Fig. 2 shows the Bouguer gravity anomaly map. The anomaly is centred
463 around an average value of 256 mGal with a standard deviation of 25 mGal. The
464 central volcanic complex is dominated by higher than average values, which produce
465 a local positive anomaly (Fig. 4) of more than 45 mGal centred at the western edge of
466 the Las Cañadas caldera, an area known as Boca Tauce (see Fig. 1C and Table 1). A 5
467 km-wide curvilinear gravity high follows the margin of the LCC wall and connects
468 Boca Tauce with La Fortaleza at the eastern boundary of the LCC. The Boca Tauce
469 gravity high correlates well with a pronounced magnetic high in the same area (et al.,
470 2007). In general, the gravity highs of the CVC correlate well with observed magnetic
471 highs extending from Boca Tauce along the LCC towards La Fortaleza (García et al.,
472 2007), as well as with a high-velocity zone (5-6 km/s) located south of the PV-PT
473 complex (Araña et al., 2000; Watts et al., 1997). The relative gravity low over PT
474 (and extending northwards) correlates with a low velocity zone (3-5 km/s) and a
475 magnetic low (García et al., 2007). Somewhat disconnected from the central high, the
476 Teno massif shows an isolated gravity high with values similar to those observed at
477 the intersection between the Dorsal ridge and the LCC. The overall impression is that
478 the CVC, and Tenerife in general, are formed by a high density core with a
479 pronounced gravity low centred in the LCC beneath Pico Teide. This area is
480 dominated by the strongest horizontal gravity gradient of about 8 mGal/km and a
481 N45ºE azimuth. The northern boundary of the Boca Tauce high coincides with a
482 break in topographic slope between the Ucanca plain and the start of the Icod valley.
483 If one were to project the north-westernmost part of the LCC wall towards the PV-PT
484 complex, the imaginary line would follow the Boca Tauce gravity high's
485 northernmost border (50 mGal isogal). Gravity values around 30 mGal dominate the

northern part of the PV-PT complex, an almost 50% decrease compared to the gravity maximum.

b. Gravity inversion

i. Homogenous background

Inversion results shown in Figures 6 and 7 are obtained using the new gravity data only. The root mean square error in the inversion is 0.42 mGal (Fig. 8). Horizontal sections through the 3-D model between 2000 m elevation and 2000 m below sea level (bsl) show a central low density body located beneath the PV-PT complex (Fig. 6). The low density feature with a decrease in density of almost 300 kg/m^3 from background values, appears to be irregularly shaped and inclined from Pico Viejo towards the NE, following the strike of the Dorsal Ridge. The body reaches its maximum width of ca. 6 km at around sea level and also extends beneath Montaña Blanca and the entire northern slope of Pico Teide (Fig. 6). Short-wavelength positive densities down to ca. 1500 m elevation appear to follow the LCC wall from its northwesternmost part anticlockwise towards La Fortaleza. This high-density structure becomes more or less coherent at 1000 to 500 m elevation, from where the structure extends to at least 1000 m below sea level. From there onwards the high-density body seems to be restricted beneath and beyond (westwards of) the Ucanca sector of the LCC. Minimal density contrasts dominate the centre of the LCC and the adjacent Santiago rift as well as along a zone opening towards the SW from the southwestern part of the LCC (particularly prominent between +500 m and -1000 m elevation). This lower density zone in the Boca Tauce high-density body (Figs. 6, 9) may have important bearings on gravity and GPS time series collected over the past years (see section 7e). Low density bodies invoked at the western and northern periphery of the surveyed area suffer from inaccuracies in the computational domain

512 (wall effects) and are thus ignored for the moment. We shall see that employing the
513 complete data set leads to a better resolution of these anomalous bodies Northwest
514 and North of the PV-PT complex.

515 Inversion of the complete data (Figs. 9 and 10) confirms the results for the
516 LCC and the PV-PT complex obtained from inversion of the new data only. The main
517 change compared with the previous inversion relates to a deterioration in inversion
518 residuals to 0.67 mGal (an almost 80% increase; Fig. 11). Again the horseshoe shaped
519 high-density body, which opens towards the NW, dominates the CVC. This body
520 follows the topographic expression of the LCC wall to a depth of ca. 1000 m bsl
521 surrounding a low-density body located beneath the PV-PT complex. Below 1000 m
522 bsl neutral densities dominate the centre of the CVC, before the high-density body
523 forms a distorted heart-shape in plan view at a depth of ca 6000 m bsl, underlying the
524 major part of the CVC. A set of high density bodies are inferred at the northern slopes
525 of the PV-PT complex, which align to form a second horseshoe shape extending from
526 1000 m elevation to at least sea level. These bodies form a more or less coherent
527 western, southern and eastern boundary of neutral density material extending
528 northward to the shoreline. The root of this body appears to extend to at least 3000 m
529 below sea level N of PT and NW of La Fortaleza forming the northern boundary of
530 the prominent central low-density body located to the south (Fig. 10). This northern
531 horseshoe-shaped body is separated (at least above sea level) from the Boca Tauce
532 body by a neutral density feature aligned along the Santiago rift. Three other
533 individual shallow low-density features with densities similar to those of the central
534 CVC are worth highlighting. One is located in the Santiago rift close to the location of
535 the most recent eruption on Tenerife (Chinyero in 1909) and directly adjacent to
536 another similar-sized low-density body to the north, whose location coincides roughly

with the inferred western edge of the Icod valley. The second is located beneath the western wall of the La Orotava valley and the third south-east of Guajara peak, along the strike of the Rocas de García spur of the LCC (see Fig. 1C). A particular common feature, despite their very low densities, is that these zones are either only shallow rooted or they narrow at depth to below the spatial resolution of the inversion. Below 8000 m bsl the up to 35 km wide high-density core dominates central Tenerife mimicking today's shape of the island at depth, while the Teno gravity high is at its largest between depths of 2000 and 6000 m bsl. Both high-density bodies stand in stark contrast to the surrounding medium with neutral densities at depths in excess of 6000 m bsl. However, this contrast is highly biased and exaggerated by assuming a background of homogeneous density.

ii. Density-stratified background

Effects of a density stratified background on inversion results become significant below sea level (Figs. 12 and 13). We obtain density contrasts in excess of 600 kg/m3 between low and high densities, being significantly skewed towards a higher density contrast for the central core of the island. As expected, at greater depth the density contrast between the background medium and the dense core decreases significantly compared to the homogeneous medium inversion results (50 vs. 220 kg/m^3, respectively) and is assumed to be closer to reality. Particular anomalous features, highlighted in the previous section up to about sea level, are also found in the new inversion and are hence not repeated here. The most obvious difference relates to the low density "depression" modelled beneath the LCC and PV-PT complex below sea level. While the homogeneous inversion gives a contrast of more than 200 kg/m^3, creating the impression of a bowl-shaped density decrease within the

562 high-density core of the island up to 5000 m bsl. (profiles f-i in Fig. 10), the stratified
563 inversion significantly decreases the maximum depth of this depression. Still
564 maintaining both a bowl-shape and a similar density contrast against the high-density
565 core, the structure now only extends to about 2000 m bsl (profiles f-i in Fig. 13).
566

567 # 7. Gravity model interpretation and discussion
568

569 ## a. General considerations
570

571 We limit our interpretation of the data to the immediate CVC and from depths
572 of 4000 m bsl upwards. The model results do not significantly alter inferences on the
573 deep structures of the CVC (> 4 km bsl), the Teno massif or the Dorsal Ridge as put
574 forth by previous studies (Ablay and Kearey, 2000; Camacho et al., 1991), since all of
575 these were based on the same gravity data set collected outside the CVC. A
576 fundamental controversy on the deep structure relates to whether the core of Tenerife
577 is formed by an uplifted basement block as suggested by Araña et al. (2000) or as a
578 result of intrusion of mafic magma forming dense gabbroic plutons (Ablay and
579 Kearey, 2000). The different theories brought forward are potentially heavily biased
580 towards the employed data modelling (full inversion in the former case as opposed to
581 forward modelling and parameter estimation in the latter), as both studies rely on the
582 same onshore gravimetric data set. It would appear necessary to include marine
583 gravity data in modelling the deep structure beneath Tenerife to obtain more
584 conclusive results.

585 The new gravity data in combination with a cleaned set of the existing data,
586 however, enables the assessment of the shallow and intermediate sub-surface

587 architecture of the CVC and its evolution in unprecedented detail and this shall be the
588 focus for the remaining part of the paper.
589 Fig. 14 identifies particular geometric features in the sub-surface density
590 distribution beneath the CVC.
591 First and foremost, the complex appears to be built on two intersecting
592 structural features:
593 i) a NE-SW striking high density ridge forming the southern part of the
594 Las Cañadas edifice with a direct link to the Dorsal Ridge and
595 ii) a NW-SE striking structure linking the Teno massif to the CVC via
596 the Santiago rift.
597 At their intersection at the SW part of the Ucanca caldera, a graben-like structure is
598 modelled by the inversion (Figs. 9, 14). This structure may have played an important
599 role during the reactivation of the complex in 2004, as explained in section 7e. This
600 graben is following the NE-SW trend described above and may be linked to a graben
601 structure exposed in deposits of the Ucanca formation in the caldera wall close to the
602 intersection of the Roques de García and the caldera wall (Galindo et al., 2005). It is
603 obvious that the intersection of these two lineaments controlled the evolution of the
604 CVC. It is interesting to note that the Dorsal Ridge appears to be linked directly with
605 the older Las Cañadas edifice and it is therefore not extending beneath the PV-PT
606 complex to intersect the Santiago rift beneath Pico Viejo as proposed earlier (Ablay et
607 al., 1998; Carracedo, 1994). The intersection is likely to be situated further south
608 within the Ucanca sector of the LCC.
609

610 ## b. The core of the CVC
611

612 The general picture emerging from the inversion results is that a high density
613 body extending from depth (in excess of 4 km bsl) to shallow levels forms the core of
614 CVC. This core appears to be partly associated with a fundamental mafic shield
615 building phase of Tenerife similar to other volcanic ocean islands. Remnants of the
616 shield are exposed at the Roques del Conde sequence, and the Teno and Anaga
617 massifs up to elevations of nearly 1000 m. Shallowing of the structure to near surface
618 levels to the west of the LCC may be attributed to the formation of the more or less
619 conical Boca Tauce volcano (Fig 12, for z = 1000m). Eruptive products of the Boca
620 Tauce volcano include lavas and pyroclastic rocks rich in mafic minerals and
621 plagioclase cumulates. Rock densities for this sequence can exceed 2900 kg/m^3 and
622 represent the densest rocks exposed nowadays at the CVC. It is thus likely that the
623 modelled density contrasts, in excess of 370 kg/m^3, are indicative of these dense rocks
624 and even denser deeper-seated plutonitic rocks including cumulates (see Ablay and
625 Kearey, 2000, for estimates on cumulate densities). The long-wavelength positive
626 magnetic anomaly detected in this area is consistent with the interpretation of an old
627 mafic volcanic edifice (Araña et al., 2000; García et al., 2007). The Boca Tauce
628 lithologies with Lower Group ages of up to 3.5 Ma are exposed in the South western
629 part of the LCC's Ucanca sector and adjacent valleys. These rocks occur also as
630 accidental fragments at the PV summit, erupted during a phreatic phase in the central
631 crater as part of the 1792 Narices del Teide fissure eruption. This highlights that a pre-
632 Las Cañadas edifice also extended beneath what is now the CVC early in the
633 evolution of Tenerife and contradicts inferences of three isolated proto-Tenerife
634 islands (Teno, Anaga and Roques del Conde; see Ancochea et al., 1990; Walter,
635 2003). As a consequence, the high-density body, modelled to extend to shallow depth
636 beneath PV, may indeed be part of the Boca Tauce edifice (Fig. 13, profile f).

637 Including both Lower and Upper Group lithologies, and thus also the Boca Tauce as
638 its westernmost entity, the Las Cañadas edifice was constructed up to 179ka. We
639 interpret the horseshoe-shaped gravity ridge, with positive density contrasts of up to
640 310 kg/m^3 following the LCC wall, as remnants of this dominant edifice. A rather
641 dramatic petrological and volcanological change occurred with the formation of
642 Upper Group lithologies which resulted from an increased in the eruption of evolved
643 phonolitic magmas and thus increasingly highly explosive volcanism. The slight
644 reduction in modelled densities along the ridge may reflect an overall reduction in the
645 bulk density of Upper Group lithologies due to the occurrence of lower density
646 magmas and lavas and a higher proportion of pyroclastic deposits during the
647 construction of the LCC.
648

649 ## c. The shallow structure of the CVC
650

651 One of the most important inferences from the models is that the shallow
652 subsurface beneath the CVC is not entirely composed of high-density material.
653 Four zones of low density appear to characterise the shallow structure beneath
654 the CVC up to surface levels:
655 i) the bowl-shaped density low beneath the PV-PT complex (discussed
656 in detail in section 7d),
657 ii) a NNE-SSW trending low density region made up by two gravity
658 lows located in the Icod valley and crossing the Santiago rift at an
659 angle of ca. 80º (Fig. 12 for z =1000 to -1000m, and Fig. 14 for z =
660 500m),

iii) a linear alignment of low density bodies connecting the Icod low density body with a low beneath the Tigaiga massif at the western border of the Orotava Valley (Figs. 12, 14), and

iv) two density lows southeast of Guajara Peak, at the southern slopes of the Las Cañadas edifice.

All four zones show similar negative density contrasts, mainly due to the general assumptions behind the inversion approach. Except for the Icod anomaly, all low density bodies appear to be shallow rooted, with maximum extension to around sea level (Figs. 12 and 14). The Icod low density body appears to be deep-rooted, extending from the ground surface to around 2000m below sea level. The area underlain by this body is dominated by mafic dykes and normal faults exposed in road cuts, which document the extensional stress field mirrored also by the abundance of young mafic cones along the Santiago rift, including the 1909 Chinyero cone. It is therefore likely that this body has a deep structural control such as a fault or damage zone potentially associated with dykes. Low densities may result from hydrothermal fluid migration creating secondary void space and alteration, corrosion and/or active fracturing and faulting along these structural elements. It also appears that this zone played an dominant role during the recent reactivation of the CVC, as discussed in more detail in section 7e.

The North-South profile A in Fig. 13, reveals the pronounced asymmetry in the distribution of high-density material between surface levels and 3000 bsl. Whereas the high density body reaches the near-surface beneath the southern portion of the LCC, the area below and north to the PV-PT complex is dominated by lower density material except for the shallow rooted horseshoe alignment of high-density material forming the northern border of the low-density interior of the PV-PT complex (Fig.

686 13). The strong N-S asymmetry has also been highlighted in seismic velocity (Watts
687 et al., 1997) and aeromagnetic data (Araña et al., 2000; García et al. 2007). It has been
688 suggested by both Araña et al. (2000) and Ablay and Kearey (2000), that these
689 anomalies are due to low density, partly chaotic and unconsolidated volcanic rocks
690 (mainly mafic and phonolitic lavas), erupted from the PV-PT complex over its
691 lifetime from 179 ka onwards. These deposits represent the major infill of the Icod
692 valley. Our model clearly supports these earlier inferences, yet we can put further
693 constraints on the destruction of the Las Cañadas edifice and the formation of the Las
694 Cañadas caldera.

695 The absence of a surface expression of a northern caldera wall has led various
696 authors to suggest that the LCC may indeed have formed as a result of a large lateral
697 mass wasting (Cantagrel et al., 1999; Ancochea et al., 1999; Watts and Masson,
698 2001). In their conceptual model, the LCC wall is the headwall of the Icod landslide
699 due to its "striking resemblance to the head scars of large landslides" (Watts and
700 Masson, 2001). While landslides undoubtedly played an important role in the
701 geological evolution of Tenerife (Ablay and Hürlimann, 2000), our investigation does
702 not find any evidence for a lateral collapse origin of the LCC. Quite the opposite, we
703 find clear evidence supporting its formation by vertical collapse.

704 First, neutral density material is not only infilling the Las Cañadas depression but also
705 extending to considerable (>2000 m bsl) depth, significantly displacing the underlying
706 high density body. This displacement requires a deep structural perturbation unlikely
707 to be induced by a surficial landslide with a maximum penetration depth of 1000 m as
708 inferred for the Icod case (Hürlimann et al., 2000). The perturbation is consistent with
709 a down faulting of a sizeable part of the high density interior of the Las Cañadas

edifice and possible alteration in the form of lateral landslides directed to the north during Lower Group times.

Second, short wavelength high-density bodies in the Diego Hernández sector, shown in Fig. 6 (for z=1500m), delineate an elliptic pattern surrounding a central neutral density body and may be interpreted as shallow intrusions. The inferred semi-major axis of this feature strikes NNW-SEE and matches electromagnetic observations in this area (Coppo et al. 2008), which identified a NNW-SSE elongated funnel-shaped conductive layer at depth. This area is also characterised by a well defined magnetic low as revealed by recent aeromagnetic data (García et al., 2007). The semi-minor axis of the elliptic alignment of the high-density bodies matches the semi-minor axis of the electromagnetic resistivity print as well as the magnetic low and we propose that these features are related, i.e., have a common source. The distribution of the high-density bodies resembles intrusions along a ring fault, which is consistent with the interpretation of the conductive layer representing the remnant of an older edifice affected by vertical collapse. The resistivity prints and the morphology of the conductive layer led Coppo et al. (2008) to propose the initiation of the collapse in the SE part of the Diego Hernández sector. The abundance of high-density bodies in that part of the caldera depression is in perfect agreement with ring fault formation and initiation of the vertical collapse there. The combination of results from these potential field investigations (gravity, magnetotellury and magnetics) provides irrefutable evidence for a vertical collapse origin of the LCC, which is also supported by the abundance of voluminous products of phonolitic explosive (caldera-forming) volcanism on the island (Martí et al., 1994; Edgar et al., 2007; Pittari et al, 2008)

It has been suggested by various authors that the head of the Icod valley is buried beneath eruptive products of the PV-PT complex (Martí et al., 1997; Martí et

al., 1998; Ablay and Hürlimann, 2000). The horseshoe-shaped alignment of shallow rooted high density bodies to the north of the complex gives the impression of a structural barrier between the complex and the topographic expression of the Icod valley, coinciding with a significant break in slope (Fig. 12, for z = 1000m; Fig. 13, profile A). One could suspect that parts of this structure represent the northern (buried) caldera wall. It is furthermore interesting to note that the maximum opening of the structure matches the maximum width of the Icod valley and we thus interpret that structure to be associated with the formation of the landslide valley. Shallow AMT resistivity prints at the northern slope of the PV-PT complex identify a dramatic shallowing of a conductive body below a resistive layer in the areas highlighted by these high density bodies (Coppo, 2007). This author interprets the conductive layer as the décollement of the Icod landslide, most probably coinciding with the El Mortalon layer, which is thought to be the gliding plane of the slide (Bravo, 1962; Cantagrel et al., 1999). We propose that some of the high density bodies represent intrusives along the (sub)vertical lateral failure planes of the slide, marking its side walls. Similar features are observed elsewhere in the form of basic magmatic intrusions along structures resulting from lateral mass wasting on ocean islands, such as Hawaii or Reunion (Oehler et al., 2004). The headwall may also be either marked by an intrusion or coincide with the remnant of the northern caldera wall. We cannot provide a conclusive answer as to the fate of the northern caldera wall and its role during the formation of the Icod valley, but all evidence points towards a remnant structure below the PV-PT complex whether it be the Icod head scar or the northern caldera wall or (probably most likely) a combination of both. The key finding here is that the headwall of the Icod valley is located well outside (to the N of) the current

caldera depression and cannot thus have had any role in the formation of the LCC wall.

d. The interior of the PV-PT complex

The interior of the PV-PT complex appears to be made up of low density material extending from close to the surface to about sea level. The horizontal extent of the density low is from Pico Viejo in the west to Montaña Blanca in the east of the complex. This marked density low has an overall irregular shape with a finger-like protrusion below PV. There are several possibilities to explain the low densities below the complex.

First, the complex is dominated by phonolitic eruptive products; mostly lava flows and pumice fall deposits with the lowest bulk densities (as low as about 1100 m^3/kg as measured in the field; see Table 2 and Ablay and Kearey (2000), as well as more primitive highly-vesiculated lavas, also with bulk densities lower than the background density.

Second, the complex may, to some extent, be hydrothermally altered and internally eroded causing secondary void space leading to lower bulk densities. Surface expressions of hydrothermal alteration zones are restricted to the area of the Roques de García, the lower part of the caldera wall and within the youngest Pico Teide summit crater. Remnants of two older Teide craters, exposed at ca. 3500 m close to the upper cable car stop, exhibit fumarolic activity at the time of this writing. The bulk density of the highly altered summit crater deposits is well below the background density. Assuming that at least parts of the interior of the complex have undergone a similar degree of alteration, one would expect lower densities for the interior of the complex, as perhaps best exemplified by the conduit-shaped low

785 density feature beneath PV extending upwards and to the west from the centre of the
786 density low (Figs. 6, 7 and 13). In fact, recent electromagnetic data show a highly
787 conductive body beneath Montaña Blanca with electrical resistivities of less than 20
788 ohm m (Coppo et al., 2008), a clear indication for either the presence of shallow
789 hydrothermal alteration or a geothermal system. With the water table being located
790 well below 400 m below the caldera floor (Gottsmann et al., 2006 and references
791 therein), i.e. < 1800 m asl, it is conceivable that large parts of the immediate
792 subsurface beneath Montaña Blanca (summit at 2800 m asl) is hydrothermally altered
793 rather than hosting saline ground water. The total extent of hydrothermal alteration of
794 the complex is not well defined but both our gravimetric as well as the AMT data
795 indicate that a rather substantial volume of the total volume of the complex of ca. 9
796 km^3 may be substantially altered and structurally weakened. Of course these findings
797 have important bearings on the stability of the complex, with northern slopes showing
798 angles of inclination of 38º or more. With a history of several landslides, the northern
799 flank of the complex is a likely locus for future mass wasting facilitated by internal
800 corrosion of the complex.

801 Petrological evidence points towards the existence of shallow magma
802 chambers (at depths of around sea level) feeding past phonolitic eruptions at the
803 complex (Ablay et al., 1998; Triebold et al., 2006; Andujar, 2007). It is possible that
804 the rather clearly defined lower boundary of the low-density body, resolved by the
805 stratified background model (Figs. 12 and 13), marks the transition from
806 hydrothermally altered material to remnant magma reservoirs. At a depth of about
807 1000 m bsl a neutral density contrast is modelled which increases with depth to a
808 contrast of ca 100 kg/m^3, forming a sizable (several km^3 in volume) bowl-shaped
809 body beneath the complex, clearly separated from the high density material forming

the core of the Las Cañadas edifice. One would expect that partially crystallised phonolitic magma would have a density similar to background densities and one could propose this region to at least host remnants of highly evolved magmatic bodies. Whether or not these bodies contain eruptable material, if defined by a critical abundance of melt, may not be resolved by the available gravimetric data.

e. Relation to recent unrest

The sub-surface density distribution allows us to put these new findings in relation to geodetic and seismic observations performed during the recent reactivation of the CVC in spring 2004 and onwards. Details on investigation strategies and results can be found in the recent papers by Gottsmann et al. (2006), Almendros et al. (2007), Fernández et al. (2007), and Martí et al. (2008a). Two features are worth highlighting.

First, the low-density body identified inside and crossing the Icod valley southwestwards (Fig. 14) underlies the zone in which the most drastic residual gravity changes were documented in the first few months of the reactivation. It is fair to assume a relationship between this deeply rooted negative density anomaly and the documented sub-surface mass changes. This area has also been recognised to undergo periodic ground deformation, as shown by recent DGPS and InSAR observations (Fernández et al., 2004). The spatio-temporal gravity changes as well as the seismic data have been interpreted to reflect aqueous fluid migration at depth during the period of reactivation. We therefore propose that the perturbation of the CVC, as documented by the various geophysical techniques, may be rooted in the low-density body. Upward movement of pressurised aqueous liquids may have been controlled by

836 pre-existing structural weaknesses. Mass addition was also documented in the Ucanca
837 sector of the LCC along the Santiago Rift (Gottsmann et al., 2006). Accounting for
838 the dominant NW-SE structural control of the CVC, linking the LCC to the Teno
839 massif, it appears reasonable that this structure controlled most of the changes at
840 depth. In fact, results from the inversion of integrated stacked DInSAR and GPS data
841 collected between 2003 and 2006 are in very good agreement with this hypothesis
842 (Fernández et al., 2008).

843 Second, a joint GPS and gravity benchmark located just outside the
844 topographical expression of the Ucanca wall underwent significant ground
845 deformation and gravity changes during the period of reactivation, which were
846 difficult to interpret (Gottsmann et al., 2006). The new gravity inversion results put
847 this benchmark inside an inferred graben structure at the intersection of the two
848 dominant structural lineaments as documented above (Figs. 6 and 9). Indeed from a
849 topographical perspective a sizeable part (> 200m length) of the Ucanca caldera wall
850 is missing in this particular area . Its dissected nature as well as the abundance of
851 slickensides on (sub)vertical surface outcrops provides geomorphological and
852 geological evidence for a tectonic control on the evolution of this part of the LCC.
853 These features are indicative for relative extension, possible graben formation and
854 structural weakening. The ground deformation and density changes observed between
855 2004 and 2005 in this area are consistent with localised
856 pressurisation/depressurisation cycles and associated mass and density changes over
857 periods of a few months or less. Fernández et al. (2008) found deformation sources
858 whose position, depth, radius, pressure and mass evolve over time. Displacements
859 occur particularly along low-density zones (including the southwestern part of the
860 Ucanca depression) and areas surrounding high-density bodies (see Fig. 14). It

appears that again shallow and localised sub-surface dynamics were controlled by the dominant structural entities of the CVC at the time of its reactivation.

8. Summary and Conclusion

We present a new set of gravimetric data from the central volcanic complex on Tenerife, which, coupled with a full 3-D data inversion, enabled unprecedented insights into the shallow sub-surface structure beneath the complex.

1. The centre of the island is dominated by a high-density core expressed by a local gravity high, which is formed by the intersection of two principal structural lineaments oriented at about right angles: the Teno-Santiago rift and the Dorsal ridge. These structures have controlled the morphological and volcanic evolution of both the island and the central complex over the past few million years and appears to continue controlling sub-surface dynamics as shown during the recent reactivation of the complex in 2004.
2. Based on a combination of gravimetric and geological data we propose the existence of a central volcanic complex early in the evolution of Tenerife. The phonolitic complex, beneath the centre of the island, most likely formed within an early shield structure. Construction of isolated volcanic edifices forming the three corners of the island is not supported by our data. The asymmetric density distribution below sea level is consistent with the removal of

885 significant proportions of the early central edifice in the form of
886 lateral landslides directed to the north during Lower Group times.
887 3. We find strong evidence for a vertical collapse origin of the Las
888 Cañadas caldera both from gravimetric data alone as well as from its
889 excellent correlation with results from recent electromagnetic and
890 aeromagnetic investigations. The distribution of small and shallow
891 high-density bodies in the Diego Hernández sector is consistent with
892 intrusions along a ring fault marking the periphery of a funnel-
893 shaped conductive layer interpreted to represent the base of the
894 Diego Hernández caldera.
895 4. A horseshoe-shaped alignment of high-density bodies at shallow
896 depth to the north of the Pico Viejo - Pico Teide complex is
897 interpreted to represent shallow intrusions into a scar left behind by
898 the Icod landslide, marking the horizontal extent of the slide as well
899 as its head wall. The head wall is nowadays buried beneath eruptive
900 products of the youngest volcanic complex on the island, and thus
901 does not relate in any way to the currently exposed LCC wall. The
902 Icod valley head wall may represent parts of the northern caldera
903 wall, formed by the superposition of three vertical collapses over the
904 past 1 Ma.
905 5. The interior of the PV-PT complex is characterised by a cylindrically
906 shaped body extending from depths of ca. 3000 m bsl to about sea
907 level. This body of neutral density is interpreted to represent the
908 current plumbing system of the complex. Above sea level, low
909 density material dominates the shallow interior of the complex and is

thought to result from a combination of evolved eruption products (dominantly phonolitic air-fall and intermediate to evolved vesiculated lavas) with a significant degree of hydrothermal alteration leading to internal corrosion.

Future geophysical investigations at the CVC aiming at resolving the temporal evolution of the sub-surface in light of the recent reactivation should take into account the results presented here. Two points are worth mentioning. First, the degree of internal alteration of the PV-PT complex needs to be better assessed and implications for slope stability need to be considered. Edifice collapse may have severe impacts in its own right but may also impact on magmatic systems at depth (Reid, 2004). Such scenarios need to be accounted for in quantitative risk assessment and monitoring programs need to provide critical baseline data.

Second, the control of the two dominant structural lineaments on the evolution of the central volcanic complex is evident throughout its history. These structures appear to define preferential pathways for both aqueous fluid and magma migration. Monitoring networks should hence include coverage of these structures in addition to the immediate PV-PT complex.

Acknowledgments

A Royal Society University Research Fellowship to JG is acknowledged. The Spanish Ministry of Education and Science funded the work via research grants TEIDEVS (CGL2004-05744-C04-02) and TEGETEIDE (CGL2004-21643-E). Research by AGC and JF was also supported by project GEOMOD (CGL2005-

937 05500-C02). JG and JM acknowledge support from a bilateral CSIC - Royal Society
938 International Joint Project. Thorough reviews were provided by J. Fonseca and D.
939 Carbone.
940

941 REFERENCES

942 Ablay, G. and Hürlimann, M., 2000. Evolution of the north flank of Tenerife by
943 recurrent giant landslides. J.Volcanol. Geotherm. Res., 103(1-4): 135-159.

944 Ablay, G. and Kearey, P., 2000. Gravity constraints on the structure and volcanic
945 evolution of Tenerife, Canary Islands. J. Geophys Res., 105: 5783-5796.

946 Ablay, G.J., Carrol, M.R., Palmer, M.R., Martí, J. and Sparks, R.S.J., 1998.
947 Basanite-Phonolite Lineages of the Teide Pico Viejo Volcanic Complex;
948 Tenerife, Canary Islands. J. Petrol., 39(5): 905-936.

949 Ablay, G.J. and Martí, J., 2000. Stratigraphy, structure, and volcanic evolution of the
950 Pico Teide-Pico Viejo Formation, Tenerife, Canary Islands. J.Volcanol.
951 Geotherm. Res., 103(1-4): 175-208.

952 Al-Chalabi, M., 1971. Some studies relating to non-uniqueness in gravity and
953 magnetic inverse problem. Geophysics, 36: 835-855.

954 Almendros, J., Ibanez, J.M., Carmona, E. and Zandomeneghi, D., 2007. Array
955 analyses of volcanic earthquakes and tremor recorded at Las Canadas
956 caldera (Tenerife Island, Spain) during the 2004 seismic activation of Teide
957 volcano. J.Volcanol. Geotherm. Res. 160(3-4): 285-299.

958 Ancochea, E., Fuster, J.M., Ibarrola, E., Coello, J., Hernan, F., Cendrerao, A.,
959 Cantagrel, J.M., and Jamond, C. 1990. Volcanic evolution of the island of
960 Tenerife (Canary Islands) in the light of new K-Ar data. J. Volcanol.
961 Geotherm. Res., 44(3-4): 231-249.

962 Ancochea, E., Huertas, M.J., Cantagrel, J.M., Coello, J., Fuster, J.M., Arnaud, N.,
963 and Ibarrola, E. 1999. Evolution of the Canadas edifice and its implications
964 for the origin of the Canadas Caldera (Tenerife, Canary Islands). J.
965 Volcanol. Geotherm. Res., 88: 177-199.

966 Andujar, J., 2007. Application of experimental petrology to the characterisation of
967 phonolitic magmas from Tenerife, Canary Islands. PhD Thesis, University
968 of Barcelona, Spain, 191 pp.
969 Aprea, C.M., Hildebrand, S., Fehler, M., Steck, L., Baldridge, W.S., Roberts, P.,
970 Thurber, C.H., and Lutter, W.J. 2002. Three-dimensional Kirchhoff
971 migration; imaging of the Jemez volcanic field using teleseismic data. J.
972 Geophys. Res., 107(B10, 2247): doi:10.1029/2000JB000097.
973 Araña, V., Camacho, A.G., García, A., Montesinos, F.G., Blanco, I., Vieira, R., and
974 Felpeto, A. 2000. Internal structure of Tenerife (Canary Islands) based on
975 gravity, aeromagnetic and volcanological data. J. Volcanol. Geotherm.
976 Res., 103(1-4): 43-64.
977 Araña, V. and Ortíz, R., 1991. The Canary Islands: tectonics, magmatism and
978 geodynamic framework. In: A.B. Kampunzu and R.T. Lubala (Editors),
979 Magmatism in extensional structural settings. The Phanerozoic African
980 Plate. Springer, Berlin, Heidelberg, New York,, pp. 209–249.
981 Barbosa, V.C.F., Silva, J.B.C. and Medeiros, W.E., 1997. Gravity inversion of
982 basements relief using approximate equality constraints on depths.
983 Geophysics, 62: 1745-1757.
984 Bosshard, E., and D. J. MacFarlane (1970), Crustal structure of the western Canary
985 Islands from seismic refraction and gravity data, J. Geophys. Res., 75,
986 4901-4918.
987 Bravo, T., 1962. El circo de Cañadas y sus dependencias. Bol. Real Soc. Esp. Hist.
988 Nat. , 40.

989 Brown, R.J. and Branney, M.J., 2004. Event-stratigraphy of a caldera-forming
990 ignimbrite eruption on Tenerife: the 273 ka Poris Formation. Bull.
991 Volcanol., 66(5): 392-416.
992 Bryan, S.E., Cas, R.A.F. and Martí, J., 1998. Lithic breccias in intermediate volume
993 ignimbrites, Tenerife (Canary Islands): constraints on pyroclastic flow
994 depositional processes. J. Volcanol. Geotherm. Res., 81: 269-296.
995 Camacho, A.G., Montesinos, F.G. and Vieira, R., 2000, A 3-D gravity inversion by
996 means of growing bodies. Geophysics, 65: 95-101.
997 Camacho, A.G., Montesinos, F.G., Vieira, R. and Arnoso, J., 2001, Modellig of crustal
998 anomalies for Lanzarote (Canary Islands) in light of gravity. Geophys. J. Int.,
999 47: 403-414.
1000 Camacho, A.G., Montesinos, F.G. and Vieira, R., 2002, A 3-D gravity inversion tool
1001 based on exploration of model possibilities. Computer and Geosciences, 28:
1002 191-204.
1003 Camacho, A.G., Nunes, J.C., Ortíz, E., França, Z. and Vieira, R., 2007, Gravimetric
1004 determination of an intrusive complex under the island of Faial (Azores).
1005 Some methodological improvements. Geophys. J. Int. 171, 478–494.
1006 Camacho, A.G., Vieira, R. and Toro, C., 1991. Microgravimetric model of the Las
1007 Cañadas caldera (Tenerife). J. Volcanol. Geotherm. Res., 47: 75-80.
1008 Cantagrel, J.-M., Arnaud, N.O., Ancochea, E., Fuster, J.M. and Huertas, M.J., 1999.
1009 Repeated debris avalanches on Tenerife and genesis of Las Canadas caldera
1010 wall (Canary Islands). Geology, 27(8): 739-742.
1011 Carlson, R.L. and Raskin, G.S., 1984. Density of the ocean crust. Nature 311: 555-
1012 558.

1013 Carracedo, J.C., 1994. The Canary Islands: An example of structural control on the
1014 growth of large oceanic-island volcanoes. J. Volcanol. Geotherm. Res.,
1015 60(3-4): 225-241.
1016 Coppo, N., 2007. Morphologies of conductive structures inside and around the Las
1017 Cañadas Caldera (Tenerife, Canary Islands) PhD Thesis, University of
1018 Neuchatel, Switzerland, 246 pp.
1019 Coppo, N., Schnegg, P.-A., Heise, W., Falco, P. and Costa, R., 2008. Multiple
1020 caldera collapses inferred from the shallow electrical resistivity signature of
1021 the Las Canadas caldera, Tenerife, Canary Islands. J. Volcanol. Geotherm.
1022 Res., 170 (3): 153-166.
1023 Edgar, C.J., Wolff, J.A., Olin, P.H., Nichols, H.J., Pittari, A., Cas, R.A.F., Reiners,
1024 P.W., Spell, T.L., and Martí, J. 2007. The late Quaternary Diego Hernández
1025 Formation, Tenerife: Volcanology of a complex cycle of voluminous
1026 explosive phonolitic eruptions. J. Volcanol. Geotherm. Res., 160(1-2): 59-
1027 85.
1028 Edgar, C.J., 2003. The Stratigraphy and Eruption Dynamics of a Quaternary
1029 Phonolitic Eruption Sequence. The Diego Hernández Formation, Tenerife,
1030 Canary Islands (Spain). PhD Thesis, Monash University, Clayton, 264 pp.
1031 Enmark, T., 1981. A versatile interactive computer program for computation and
1032 automatic optimization of gravity models. Geoexploration, 19: 47-66.
1033 Fernández, J., Samsonov, S., Camacho, A.G., González, P.J., Prieto, J.F., Tiampo,
1034 K.F., Rodriguez-Velasco, G., Tunini, L., Willert, V., Charco, M.,
1035 Mallorquí, J.J., Carrasco, D., 2008. Integration of two line-of-sights
1036 classical DInSAR and GPS data to study the 2004-2006 Tenerife volcanic
1037 unrest. Geophys. Res. Abstracts, 10, EGU2008-A-10611.

Fernández, J., Camacho, A.G., P.J. González, Samsonov, S. Prieto, J.F., Tiampo, K.F., Gottsmann, J., Puglisi, G., Guglielmino, J., Mallorquí, J.J., Tunini, L., Willert, V., Rodríguez-Velasco, G., Charco, M., Navarrete, D., Duque, S., Carrasco, D., and Blanco-Sánchez, P. 2007. Tenerife island (Canaries, Spain) unrest, 2004-2006, studied via integrated geodetic observations. In: The 2007 International Geohazards Week, 5-9 November 2007. Frascati, Italy. ESA-ESRIN.

Fernández, J., Gonzales-Matesanz, F.J., Prieto, J.F., Staller, A., Alonso-Medina, A., and Charco, M. 2004. GPS Monitoring in the N-W Part of the Volcanic Island of Tenerife, Canaries, Spain: Strategy and Results. Pure and Applied Geophysics, 161: doi:10.1007/s00024-00004-02509-00022

Galindo, I., Soriano, C., Martí, J. and Perez, N., 2005. Graben structure in the Las Canadas edifice (Tenerife, Canary Islands): implications for active degassing and insights on the caldera formation. J. Volcanol. Geotherm. Res., 144(1-4): 73-87.

García-Abdeslem, J., 2000. 2-D inversion of gravity data using sources laterally bounded by continuous surfaces and depth-dependent density. Geophysics, 65, 1128-1141.

García, A., Chiappini, M., Blanco-Montenegro, I., Carluccio, R., D'Ajello Caracciolo, F., De Ritis, R., Nicolosi, I., Pignatelli, A., Sánchez, N., and Boschi, E., High Resolution Magnetic Anomaly Map of Tenerife, Canary Islands, Eds. M. Chiappini & A. García, Ann. Geophys., Vol. 50, N. 5, 2007, in press.

García, A., Vila, J., Ortíz, R., Macia, R., Sleeman, R., Marrero, J.M., Sanchez, N., Tarraga, M., and Correig, A.M. 2006. Monitoring the reawakening of Canary Islands' Teide Volcano. Eos Trans. AGU, 87 (61).

Gottsmann, J., Wooller, L.K., Martí, J., Fernandez, J., Camacho, A.G., Gonzalez, P., García, A., and Rymer, H. 2006. New evidence for the reactivation of Teide volcano. Geophys. Res Lett., 33, (L20311): doi10.1029/2006GL027523.

Guidarelli, M., Sarao, A. and Panza, G.F., 2002. Surface wave tomography and seismic source studies at Campi Flegrei (Italy). Phys. Earth Planet. Inter., 134(3-4): 157-173.

Hammer, S., 1939. Terrain corrections for gravimeter stations. Geophysics, 4: 184-194.

Hürlimann, M., García-Piera, J.O. and Ledesma, A., 2000. Causes and mobility of large volcanic landslides: application to Tenerife, Canary Islands. J. Volcanol. Geotherm. Res., 103(1-4): 121-134.

MacFarlane, D.J. and Ridley, W.I., 1968. An interpretation of gravity data for Tenerife, Canary Islands. Earth Planet. Sci. Lett., 4: 481-486.

Martí, J., Ortíz, J., Gottsmann, J., García, A. and De La Cruz-Reina, S., 2008a. Defining unrest, assessing hazards and mitigating risks during the reawakening of the central volcanic complex on Tenerife, Canary Islands (2004-2007). J. Volcanol. Geotherm. Res., accepted for publication.

Martí, J., Geyer, A., Folch, A. and Gottsmann, J., 2008b. Experimental, numerical and geophysical modelling of collapse calderas: a review. In: J. Gottsmann and J. Martí (Editors), Caldera Volcanism: Analysis, Modelling and Response. Develop. Volcanol., 10: 233-284, Elsevier, Amsterdam.

1086 Martí, J. and Gudmundsson, A., 2000. The Las Canadas caldera (Tenerife, Canary
1087 Islands): an overlapping collapse caldera generated by magma-chamber
1088 migration. J. Volcanol. Geotherm. Res., 103(1-4): 161-173.
1089 Martí, J., Hürlimann, M., Ablay, G. and Gudmundsson, A., 1998. Vertical and
1090 lateral collapses on Tenerife (Canary Islands) and other volcanic ocean
1091 islands: Reply. Geology, 26(9): 862-863.
1092 Martí, J., Hürlimann, M., Ablay, G. and Gudmundsson, A., 1997. Vertical and
1093 lateral collapses on Tenerife (Canary Islands) and other volcanic ocean
1094 islands. Geology, 25(9): 879-882.
1095 Martí, J., Mitjavila, J. and Villa, I.M., 1994. Stratigraphy, structure and
1096 geochronology of the Las Canadas caldera (Tenerife, Canary Islands).
1097 Geol. Mag., 131: 715-727.
1098 Morelli, C., Gantar, C., Honkasalo, T., McConnel, R.K., Tanner, J.G., Szabo, B.,
1099 Uotila, U., Whalen, C.T., 1974. The International Gravity Standardization
1100 Net 1971 (IGSN71), Special Publication No. 4, International Association of
1101 Geodesy, Paris.
1102 Masturyono, McCaffrey, R., Wark, D.A., Roecker, S.W., Fauzi Ibrahim, G., and
1103 Sukhyar 2001. Distribution of magma beneath Toba caldera complex, north
1104 Sumatra, Indonesia, constrained by three-dimensional P wave velocities,
1105 seismicity, and gravity. Geochem. Geophys. Geosys., 2: 2000GC000096.
1106 Nagihara, S. and Hall, S.A., 2001, Three-dimensional gravity invesion using
1107 simulated annealing: Constraints on the diapiric roots of allochthonous salt
1108 structures. Geophysics, 66: 1438-1449.
1109 Nettleton, L.L., 1939. Determination of density for reduction of gravimeter
1110 observations. Geophysics, 4: 176–183

Oehler, J.-F., Labazuy, P. and Lénat, J.-F., 2004. Recurrence of major flank landslides during the last 2-Ma-history of Reunion Island. Bull. Volcanol., 66(7): 585 - 598.

Pedersen, L.B., 1979. Constrained Inversion of Potential Field Data. Geophys. Prospect., 27: 726-748.

Reid, M. E. (2004), Massive collapse of volcano edifices triggered by hydrothermal pressurization, Geology, 32, 373-376.

Sanders, C.O., Ponko, S.C., Nixon, L.D. and Schwartz, E.A., 1995. Seismological evidence for magmatic and hydrothermal structure in Long Valley Caldera from local earthquake attenuation and velocity tomography. J. Geophys. Res., 100(5): 8311-8326.

Sandwell, D. T., and W. H. F. Smith (1997), Marine gravity anomaly from Geosat and ERS 1 satellite altimetry, J. Geophys. Res., 102, 10039-10054.

Schwiderski, E., 1980. On charting global ocean tides. Rev. Geophys. Space Phys. , 18: 243–268.

Silva, J.B.C. and Hohmann, G.W., 1983. Nonlinear magnetic inversion using a random search method. Geophysics, 46: 1645-1658.

Smith, W.H.F. and Sandwell, D.T., 1997. Global seafloor topography from satellite altimetry and ship depth soundings Science, 277: 1957-1962.

Tarantola, A., 1988. The inverse problem theory: Methods for data fitting and model parameter estimation. Elsevier, Amsterdam, 613 pp.

Tárraga, M., Carniel, R., Ortíz, R., Marrero, J.M. and García, A., 2006. On the predictability of volcano-tectonic events by low frequency seismic noise analysis at Teide-Pico Viejo volcanic complex, Canary Islands. Nat. Haz.Earth Sys. Sci., 6: 365-376.

1136 Triebold, S., Kronz, A. and Worner, G., 2006. Anorthite-calibrated backscattered
1137 electron profiles, trace elements, and growth textures in feldspars from the
1138 Teide-Pico Viejo volcanic complex (Tenerife). J. Volcanol. Geotherm.
1139 Res., 154(1-2): 117-130.
1140 Walter, T.R., 2003. Buttressing and fractional spreading of Tenerife, an
1141 experimental approach on the formation of rift zones. Geophys. Res Lett.,
1142 30(6): 1296, doi:10.1029/2002GL016610.
1143 Watts, A. and Masson, D., 2001. New sonar evidence for recent catastrophic
1144 collapses of the north flank of Tenerife, Canary Islands. Bull. Volcanol.,
1145 63(1): 8-19.
1146 Watts, A.B., Peirce, C., Collier, J., Dalwood, R., Canales, J.P., and Henstock, T.J.
1147 1997. A seismic study of lithospheric flexure in the vicinity of Tenerife,
1148 Canary Islands. Earth Planet. Sci. Lett., 146(3-4): 431-447.
1149
1150

Table and figure captions

Table 1: Simplified stratigraphic scheme for the island of Tenerife, showing the major constructive and destructive episodes. * indicates major vertical collapse, † indicates major lateral collapse (landslide). Modified and simplified after Edgar (2003).

Table 2: Measured bulk densities of lithologies exposed at the Central Volcanic Complex. Values taken from Ablay and Kearey (2000).

Figure 1. A) Location of Canary Islands off African West coast. B) Topographic models of Tenerife (28.32˚N, 16.57˚ W) showing main structural units (B and C) and locations of new gravity benchmarks (squares in C). Coordinates in B) and C) are given in UTM (m). Key to (B): Dorsal R. = Dorsal Ridge, Icod V. = Icod Valley, LCC = Las Cañadas caldera, OV =La Orotava Valley, Santiago R. = Santiago Rift, R. del Conde =Roque del Conde, PV-PT = Pico Viejo – Pico Teide complex, Tg = Tigaiga massif.

Key to (C): BT = Boca Tauce, GP = Guajara Peak, LF = La Fortaleza, MB = Montaña Blanca, PT = Pico Teide, PV = Pico Viejo, RdG = Roques de García, SR = Santiago, Rift, sectors of the Las Cañadas caldera (with decreasing age): UC = Ucanca, GJ = Guajara, DH = Diego Hernández.

Figure 2. Bouguer anomaly (mGal) map of Central Tenerife. Points indicate location of benchmarks selected for inversion of gravity data. Coordinates given in UTM (m).

Figure 3. The optimal theoretical terrain density corresponds to the density giving the minimum correlation between short-wave components of topography and gravity for distances up to a radius r around any given benchmark. The graph shows the relationship between terrain density and average radius r (bold line). A terrain density value of 2200 (kg/m^3), indicated by the thick line, is finally chosen, accounting for both the low correlation between short wave components and measured rock densities reported in Table 2.

Figure 4. Local gravity anomaly for the central volcanic complex, obtained by subtracting a general linear SE-NW trend of 0.27 mGal/km with azimuth N113ºE from the local Bouguer anomaly. This local anomaly data is employed for data inversion.

Figure 5. Sensitivity test of the inversion methodology based on a simulation of an anomalous density body located beneath the CVC. a) shows Bouguer gravity anomaly caused by the anomalous body at the benchmarks shown by black and grey circles. b) Plan view and vertical cross section of the simulated body with vertical S-shape geometry. c) Resulting 3D model from the inversion. Tick mark separation in a) –c) on all axes is 2000 m. Distortions of the inverted structure compared to the simulated body arise from data distribution and from the tendency of the inversion method to produce rounded, smoothed structures, particularly for deep (> 6 km) and peripheral zones, for which cell sensitivity is lower.

1207 Figure 6. Horizontal sections at selected depths through the 3-D model of density
1208 contrasts (kg/m^3) beneath the CVC employing local gravity anomaly data from 323
1209 new gravity measurements. A homogeneous background density is assumed for data
1210 inversion. Circle marks graben-like structure within the Boca Tauce high density body
1211 (see section 7 for discussion).
1212
1213 Figure 7: Vertical W-E profiles (a to g) and one S-N profile (A) through the 3D model
1214 of density contrasts (kg/m^3) beneath the CVC from inversion of 323 new gravity
1215 measurements. Horizontal section indicates trail lines of profiles. Model is based on
1216 assuming a homogeneous density background.
1217
1218 Figure 8: Inversion statistics for inversion of data from 323 new gravity
1219 measurements presented in Figs. 6 and 7. Root mean square inversion residual is 420
1220 μGal = 0.42 mGal.
1221
1222 Figure 9: Horizontal sections at selected depths through the 3-D model of density
1223 contrasts (kg/m^3) beneath the CVC. A homogeneous background density is assumed
1224 for data inversion. Circle marks graben-like structure within the Boca Tauce high
1225 density body (see section 7 for discussion).
1226
1227 Figure 10. Vertical W-E profiles (a to k) and one S-N profile (A) through the 3D
1228 model of density contrasts (kg/m^3) beneath the CVC. Horizontal section indicates trail
1229 lines of profiles.
1230

1231 Figure 11. Inversion statistics for inversion results presented in Fig. 9. Root mean
1232 square inversion residual is 0.67 mGal.
1233
1234
1235 Figure 12. Horizontal sections at selected depths through the 3-D model of density
1236 contrasts (kg/m^3) derived by assuming a density-stratified background beneath the
1237 CVC.
1238
1239
1240 Figure 13. Vertical W-E profiles (a to k) and one S-N profile (A) through the 3D
1241 model of density contrasts (kg/m^3) beneath the CVC. Horizontal section indicates trail
1242 lines of profiles. Model is based on assuming a density-stratified background.
1243
1244
1245
1246
1247 Figure 14: Dominant density anomalies characterising the shallow parts beneath the
1248 CVC include i) a NE-SW striking high density ridge forming the southern part of the
1249 Las Cañadas edifice with a direct link to the Dorsal Ridge (DR) and a NW-SE striking
1250 structure linking the Teno massif to the CVC via the Santiago rift (both marked by
1251 lines); ii) two low density bodies (encircled) including (i) the bowl-shaped density
1252 low beneath the PV-PT complex, (ii) a NNE-SSW trending low density region located
1253 in the Icod valley and crossing the Santiago rift, (iii) a line density lows connecting
1254 the Icod low to the Tigaiga massif (Tg), and (iv) two density lows to the south of the
1255 caldera wall. At depths > 3000 m bsl the high-density core of the CVC resembles the
1256 outline of the current island.
1257 Squares in image Z=-1000 m indicate surface projections of positions of ground
1258 deformation sources between 2003 and 2006 (Fernández, et al., 2008). It is interesting

1259 to note that most source locations are found in areas defined by shallow subsurface
1260 negative density anomalies and/or along major structural building blocks of the CVC.
1261 See Fig. 12 for scale of density contrasts.

Figure and Tables
Click here to download Figure(s): StrucGrav_Tenerife_draft180608_Figures.doc

TABLE 1

Post- shield Volcanism	Historic eruptions (e.g. Chinyero 1909)				
	Flank Eruptions: Dorsal Series (1.8 Ma-)		Central Volcanic Complex: PV-PT Formation	Pico Viejo series 2 Pico Teide series 2 Pico Viejo series 1 Pico Teide series 1 Early episode	
	Flank Eruptions: Santiago Series (0.3 Ma-)		Las Cañadas Edifice: Upper Group	* Climatic caldera collapse (0.18 Ma)	† Icod landslide (0.2-0.13 Ma)
				Diego Hernández Formation (0.57 - 0.18 Ma)	
				* Climatic caldera collapse (0.57 Ma)	† La Orotava landslide (0.57 -0.54 Ma)
				Guajara Formation (0.85 - 0.57 Ma)	† Güimar landslide (0.83 -0.57 Ma)
				* Climatic caldera collapse (1.07 Ma?)	
				Ucanca Formation (1.57 - 1.07 Ma)	
			Las Cañadas Edifice: Lower Group	**Lower Group sequence (3.8 - 1.57 Ma)** Roques de Gracia Montón de Trigo Las Pilas El Cedro El Cabezón Boca Tauce volcano (3.8 - 3.5 Ma)	
Shield construction				**Old Basaltic Series**	
				Roque Del Conde Massif (11.6 - 3.5 Ma)	Teno Massif (6.7 - 5 Ma) † Teno landslide (5.6 Ma?)
					Anaga massif (6.5 - 3.3 Ma) † Anaga landslide (~ 6 Ma)

TABLE 2

Rock type	Bulk density (m^3/kg)
phonolitic pumice fall	1080
phonolitic pumice	1390
phonolitic ignimbrite	2540
phonolitic lava	2350
phonolitic obsidian	2200
intermediate lava	2230
historic basalt	2890
mean	2201
stdev	271

FIGURES

Figure 1a

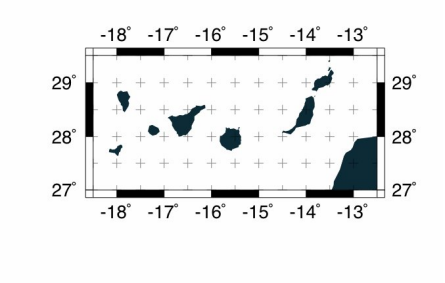

Figure 1b

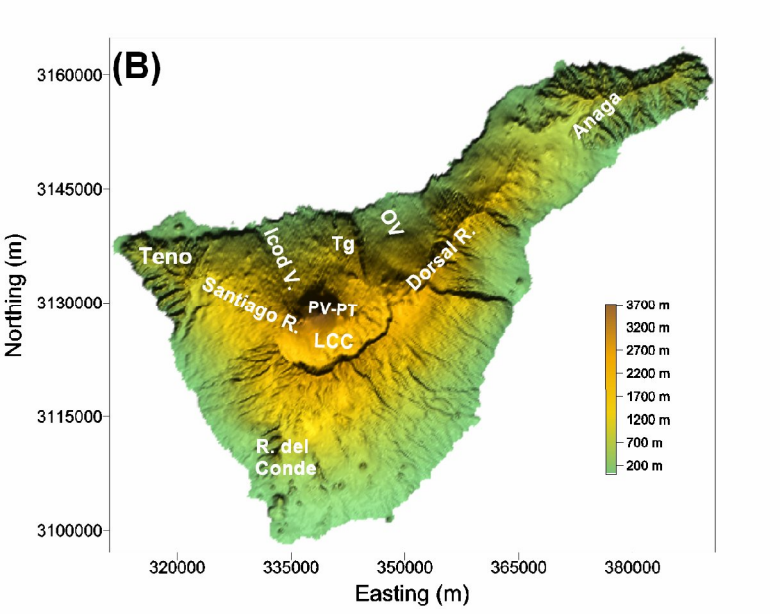

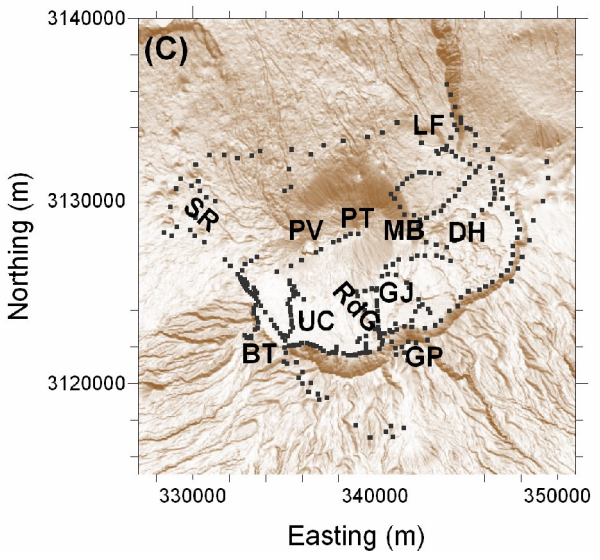

Figure 1c

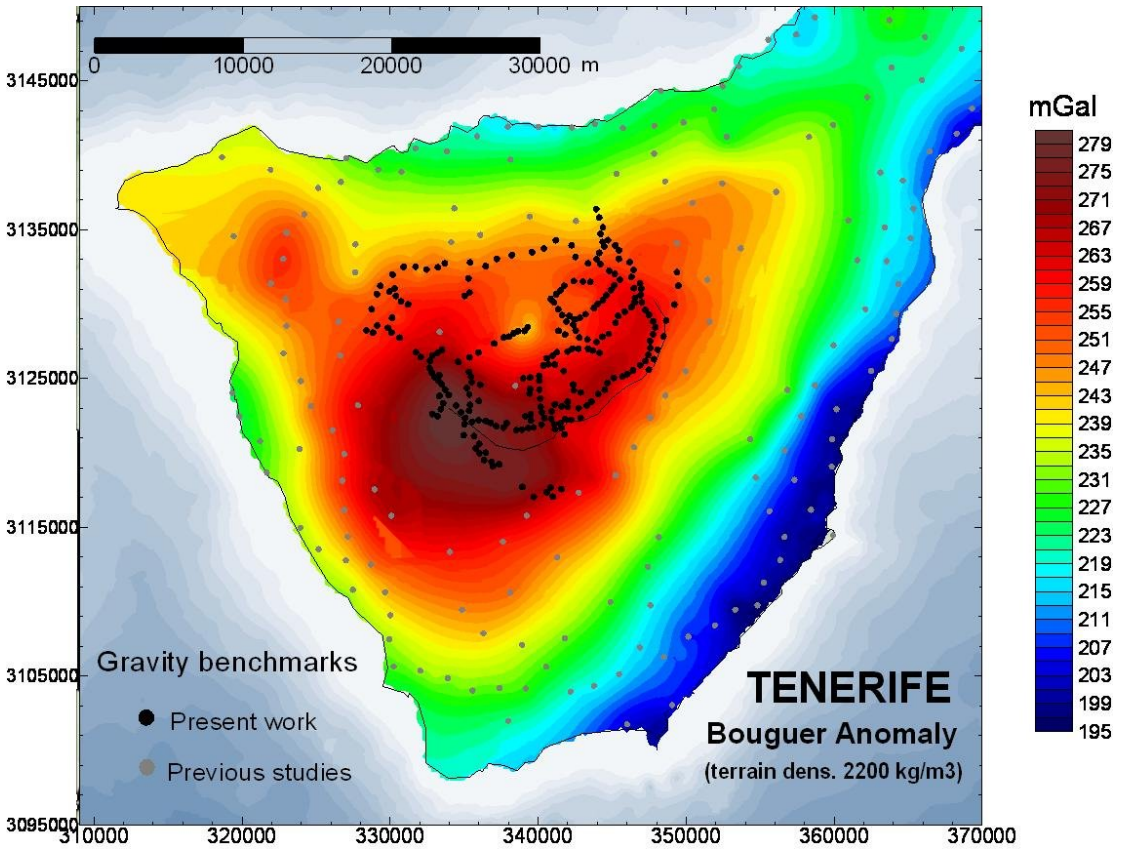
0
10000
20000
30000 m
3145000
3135000
3125000
3115000
3105000
3095000
310000
320000
330000
340000
350000
360000
370000
Gravity benchmarks
Present work
Previous studies
TENERIFE
Bouguer Anomaly
(terrain dens. 2200 kg/m3)
mGal
279
275
271
267
263
259
255
251
247
243
239
235
231
227
223
219
215
211
207
203
199
195

Figure 2

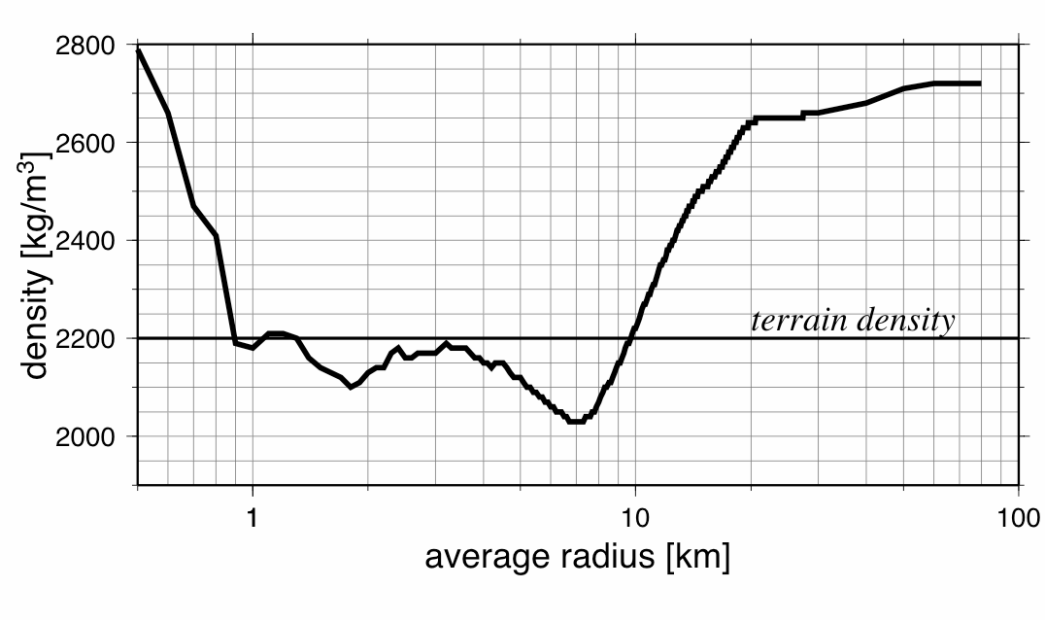
2800
2600
2400
2200
2000
density [kg/m3]
terrain density
1
10
100
average radius [km]

Figure 3

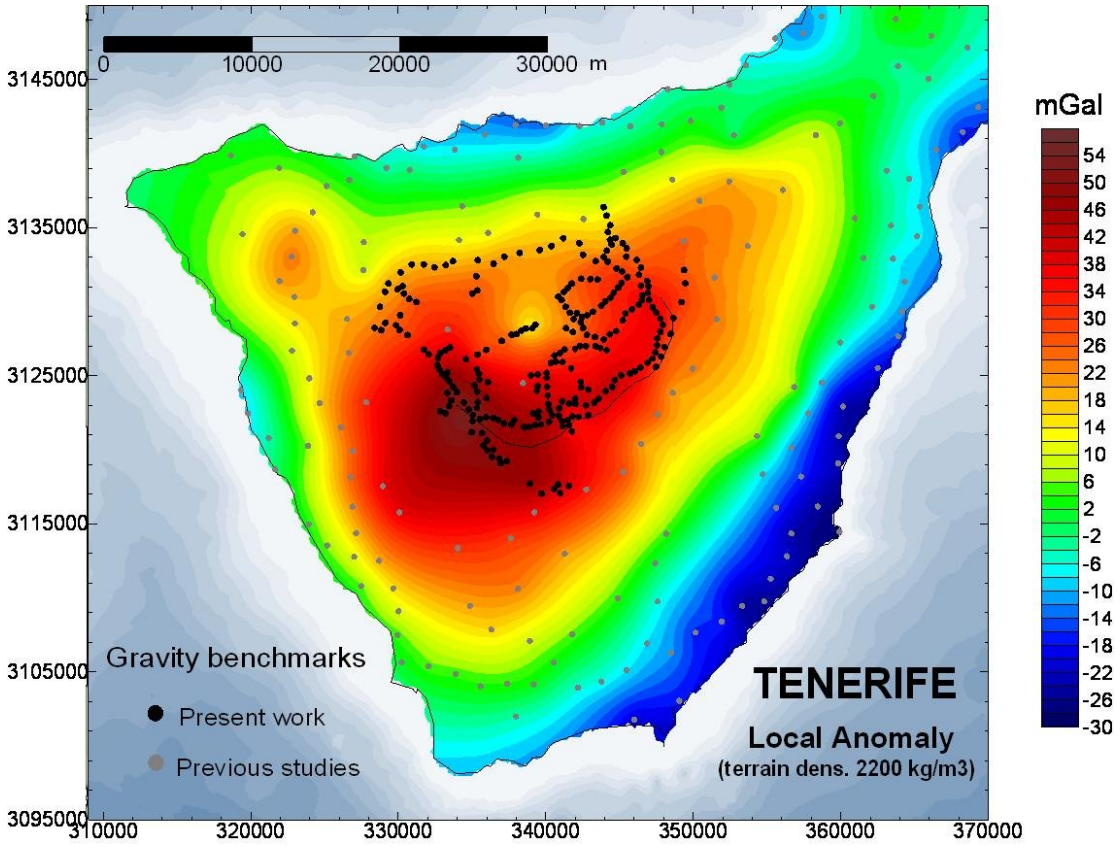
0
10000
20000
30000 m
3145000
3135000
3125000
3115000
3105000
3095000
310000
320000
330000
340000
350000
360000
370000
mGal
54
50
46
42
38
34
30
26
22
18
14
10
6
2
-2
-6
-10
-14
-18
-22
-26
-30
Gravity benchmarks
Present work
Previous studies
TENERIFE
Local Anomaly
(terrain dens. 2200 kg/m3)

Figure 4

Figure 5

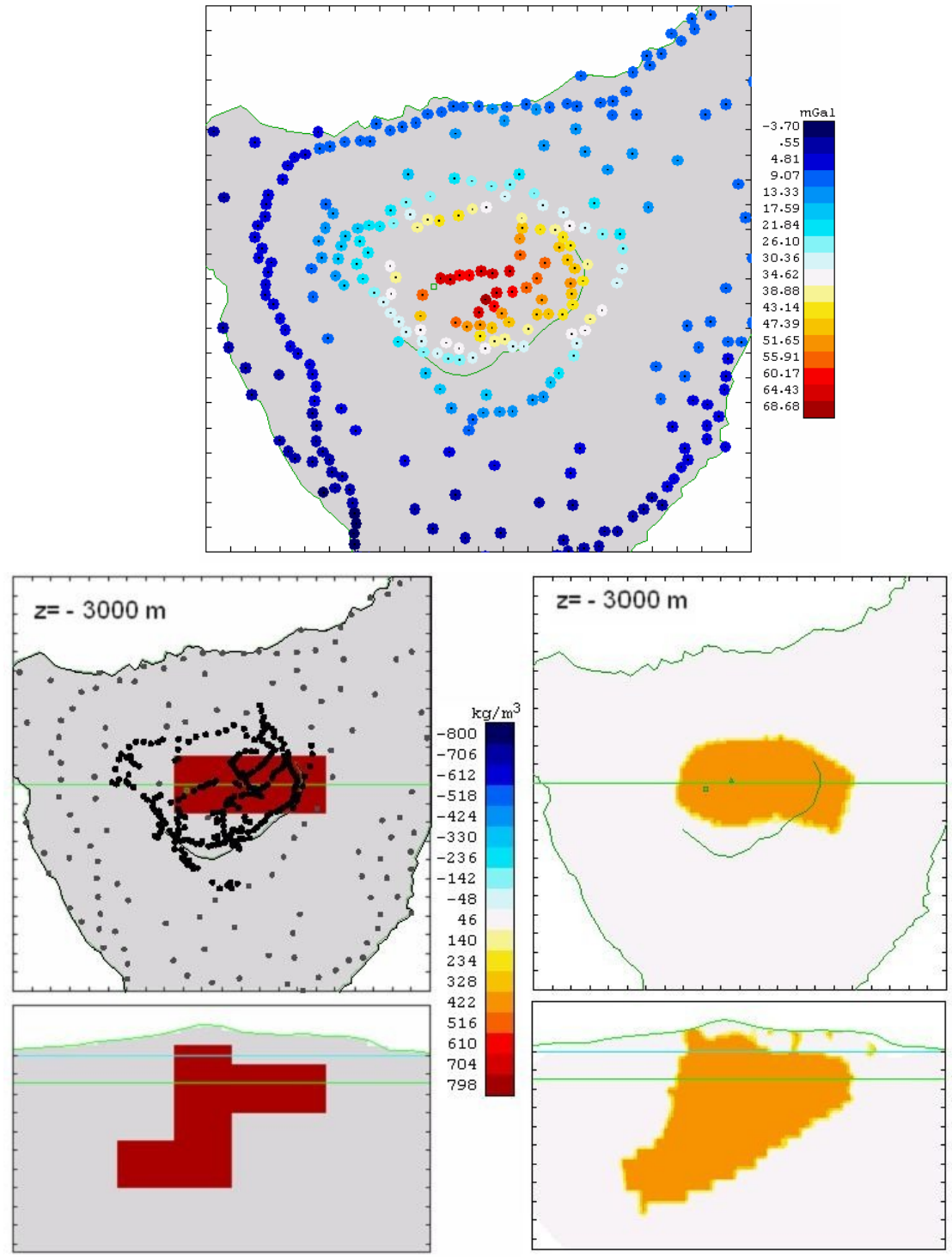
mGal
-3.70
.55
4.81
9.07
13.33
17.59
21.84
26.10
30.36
34.62
38.88
43.14
47.39
51.65
55.91
60.17
64.43
68.68
z= - 3000 m
kg/m3
-800
-706
-612
-518
-424
-330
-236
-142
-48
46
140
234
328
422
516
610
704
798
z= - 3000 m

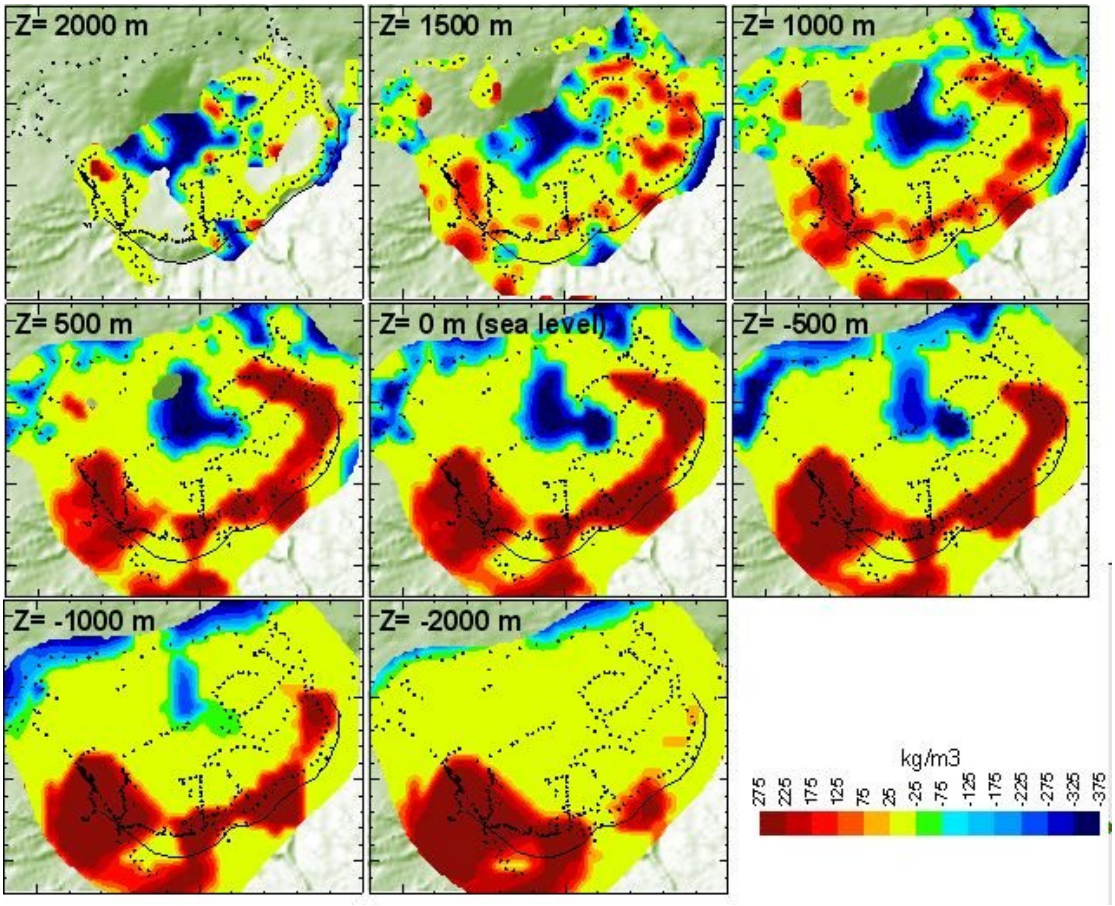
Z= 2000 m
Z= 1500 m
Z= 1000 m
Z= 500 m
Z= 0 m (sea level)
Z= -500 m
Z= -1000 m
Z= -2000 m
kg/m3
275
225
175
125
75
25
-25
-75
-125
-175
-225
-275
-325
-375

Figure 6

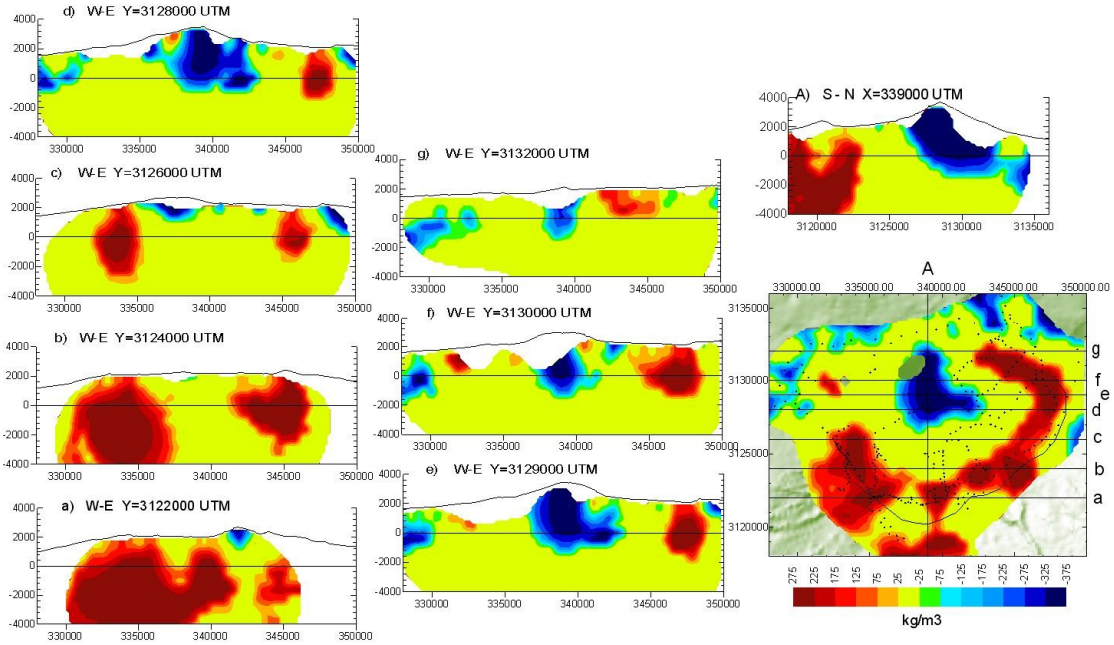
d) W-E Y=3128000 UTM
c) W-E Y=3126000 UTM
b) W-E Y=3124000 UTM
a) W-E Y=3122000 UTM
g) W-E Y=3132000 UTM
f) W-E Y=3130000 UTM
e) W-E Y=3129000 UTM
A) S - N X=339000 UTM
A
g
f
e
d
c
b
a
kg/m3

Figure 7

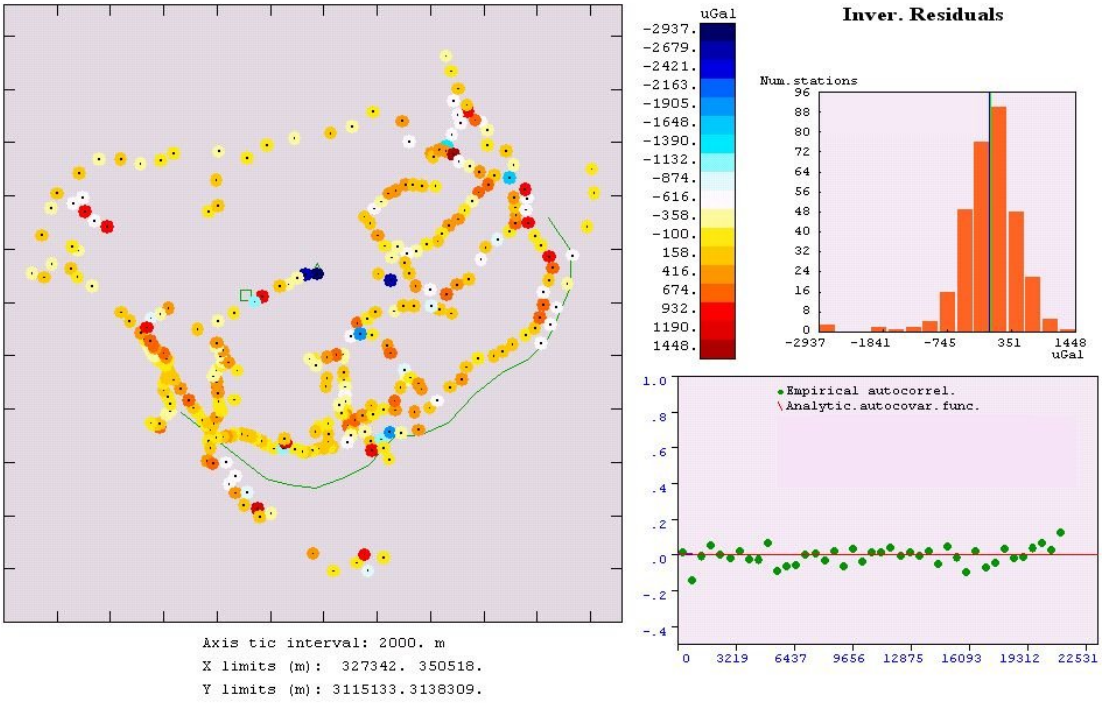
uGal
-2937.
-2679.
-2421.
-2163.
-1905.
-1648.
-1390.
-1132.
-874.
-616.
-358.
-100.
158.
416.
674.
932.
1190.
1448.
Inver. Residuals
Num.stations
96
88
80
72
64
56
48
40
32
24
16
8
0
-2937
-1841
-745
351
1448
uGal
1.0
.8
.6
.4
.2
.0
-.2
-.4
Empirical autocorrel.
\Analytic.autocovar.func.
0
3219
6437
9656
12875
16093
19312
22531
Axis tic interval: 2000. m
X limits (m): 327342. 350518.
Y limits (m): 3115133.3138309.

Figure 8

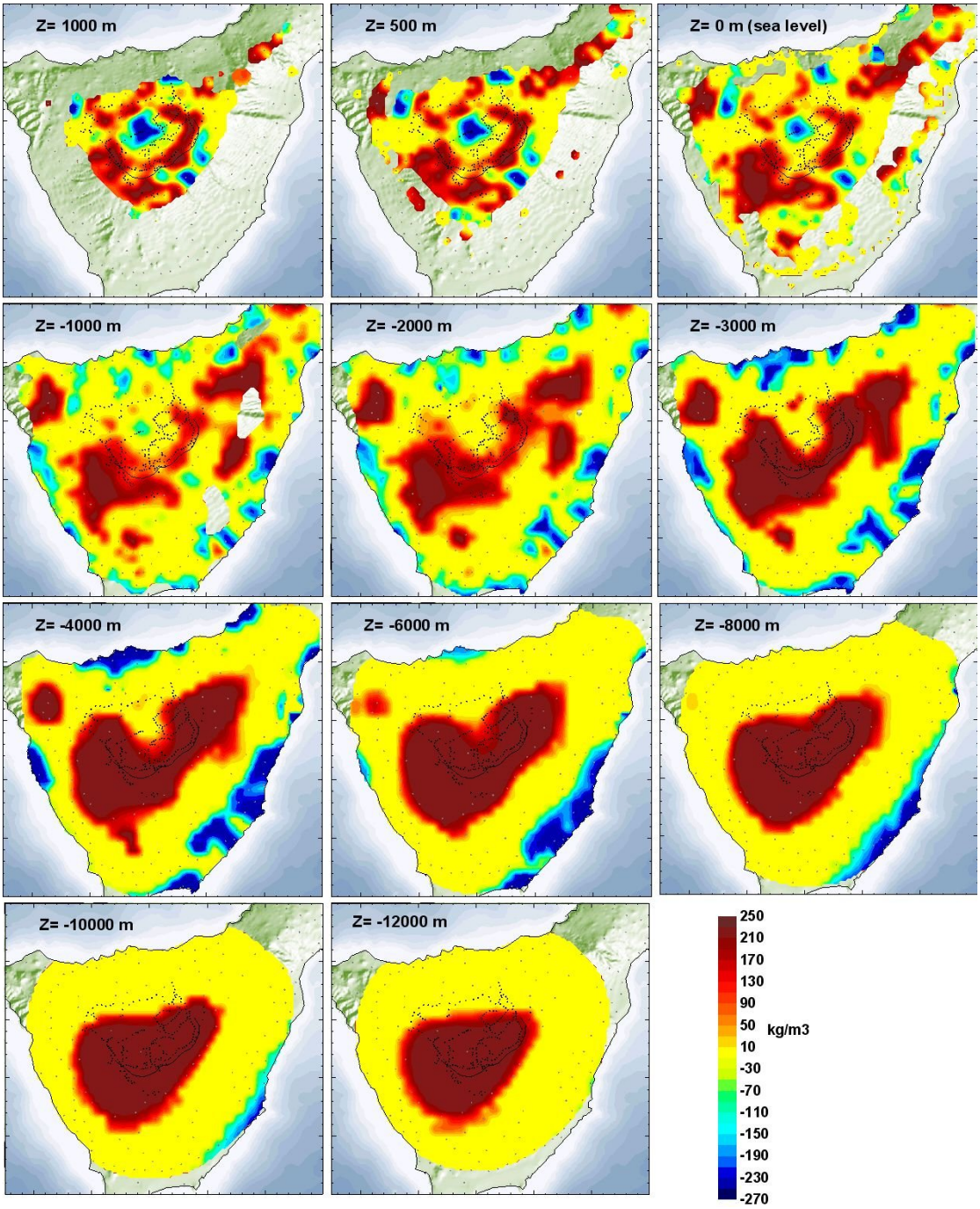
Z= 1000 m
Z= 500 m
Z= 0 m (sea level)
Z= -1000 m
Z= -2000 m
Z= -3000 m
Z= -4000 m
Z= -6000 m
Z= -8000 m
Z= -10000 m
Z= -12000 m
250
210
170
130
90
50
10
-30
-70
-110
-150
-190
-230
-270
kg/m3

Figure 9

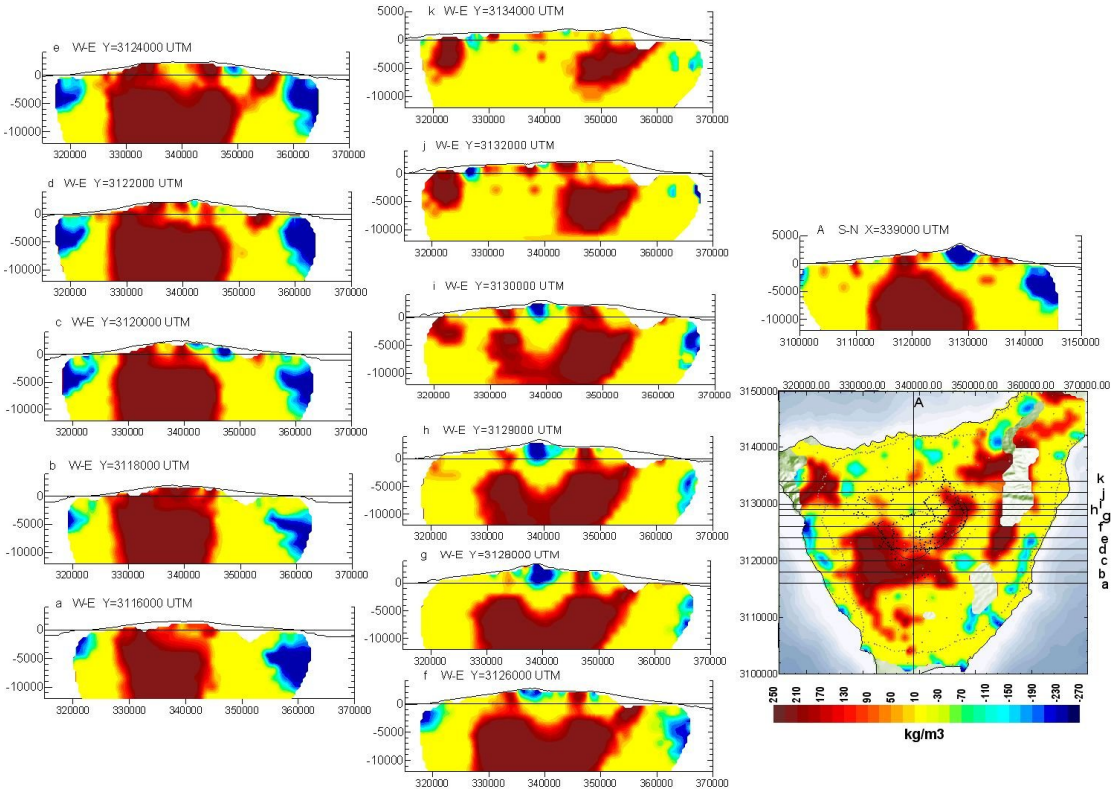
k W-E Y=3134000 UTM
e W-E Y=3124000 UTM
j W-E Y=3132000 UTM
d W-E Y=3122000 UTM
A S-N X=339000 UTM
i W-E Y=3130000 UTM
c W-E Y=3120000 UTM
h W-E Y=3129000 UTM
b W-E Y=3118000 UTM
g W-E Y=3128000 UTM
a W-E Y=3116000 UTM
f W-E Y=3126000 UTM
kg/m3

Figure 10

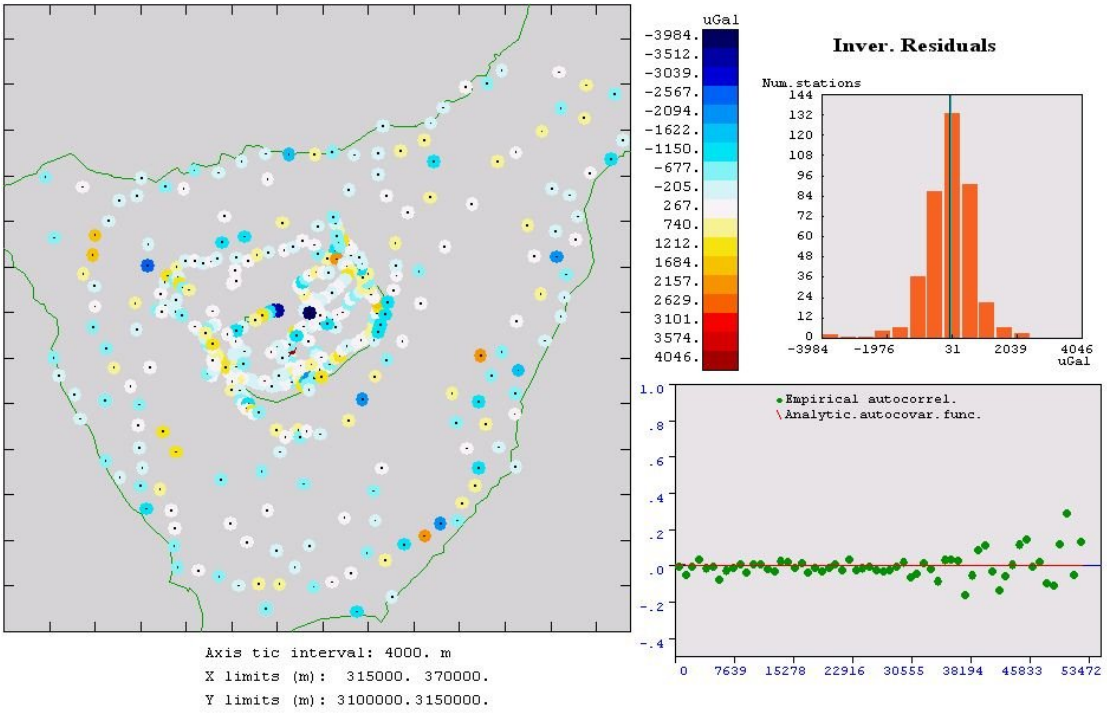
uGal
-3984.
-3512.
-3039.
-2567.
-2094.
-1622.
-1150.
-677.
-205.
267.
740.
1212.
1684.
2157.
2629.
3101.
3574.
4046.
Inver. Residuals
Num.stations
144
132
120
108
96
84
72
60
48
36
24
12
0
-3984
-1976
31
2039
4046
uGal
1.0
.8
.6
.4
.2
.0
-.2
-.4
Empirical autocorrel.
Analytic.autocovar.func.
0
7639
15278
22916
30555
38194
45833
53472
Axis tic interval: 4000. m
X limits (m): 315000. 370000.
Y limits (m): 3100000. 3150000.

Figure 11

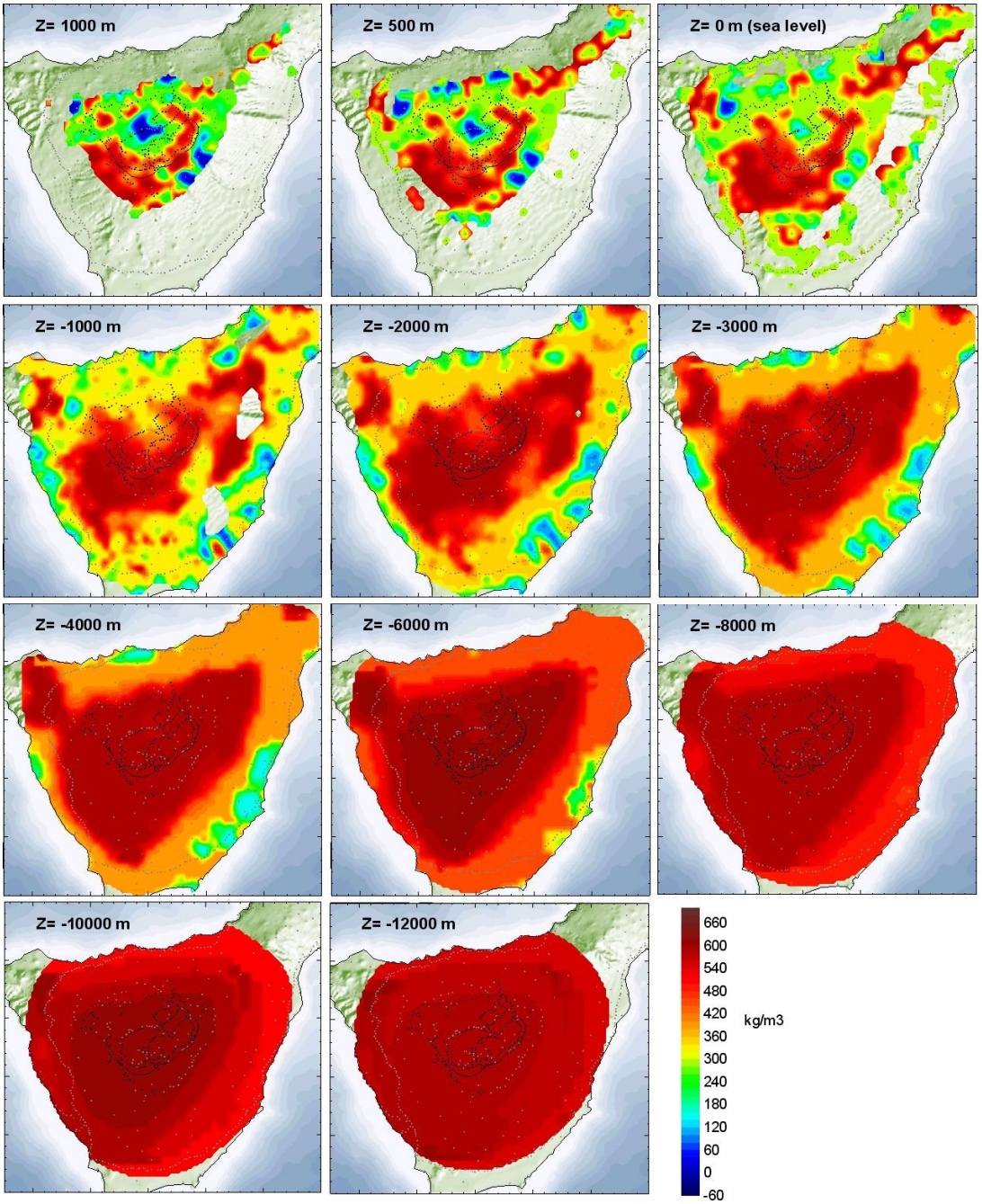
Z= 1000 m
Z= 500 m
Z= 0 m (sea level)
Z= -1000 m
Z= -2000 m
Z= -3000 m
Z= -4000 m
Z= -6000 m
Z= -8000 m
Z= -10000 m
Z= -12000 m
660
600
540
480
420
360
300
240
180
120
60
0
-60
kg/m3

Figure 12

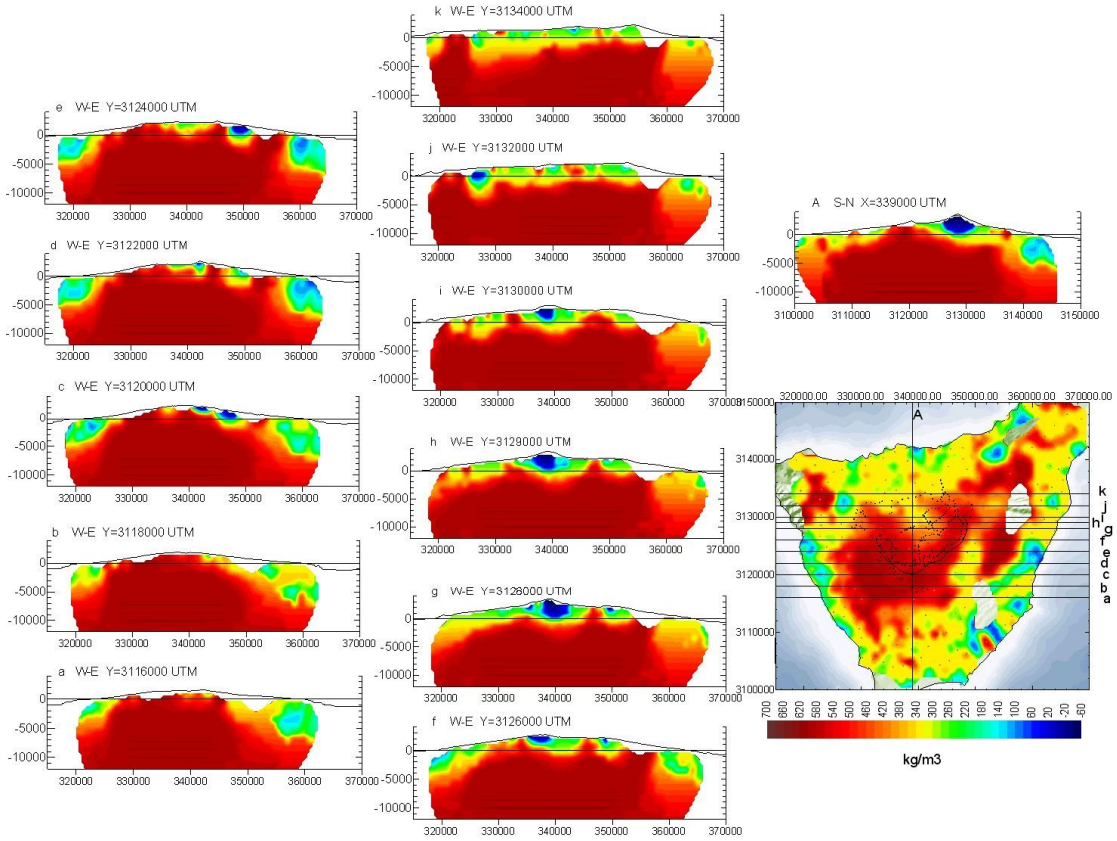
k W-E Y=3134000 UTM
e W-E Y=3124000 UTM
j W-E Y=3132000 UTM
A S-N X=339000 UTM
d W-E Y=3122000 UTM
i W-E Y=3130000 UTM
c W-E Y=3120000 UTM
h W-E Y=3129000 UTM
b W-E Y=3118000 UTM
g W-E Y=3128000 UTM
a W-E Y=3116000 UTM
f W-E Y=3126000 UTM
kg/m3

Figure 13

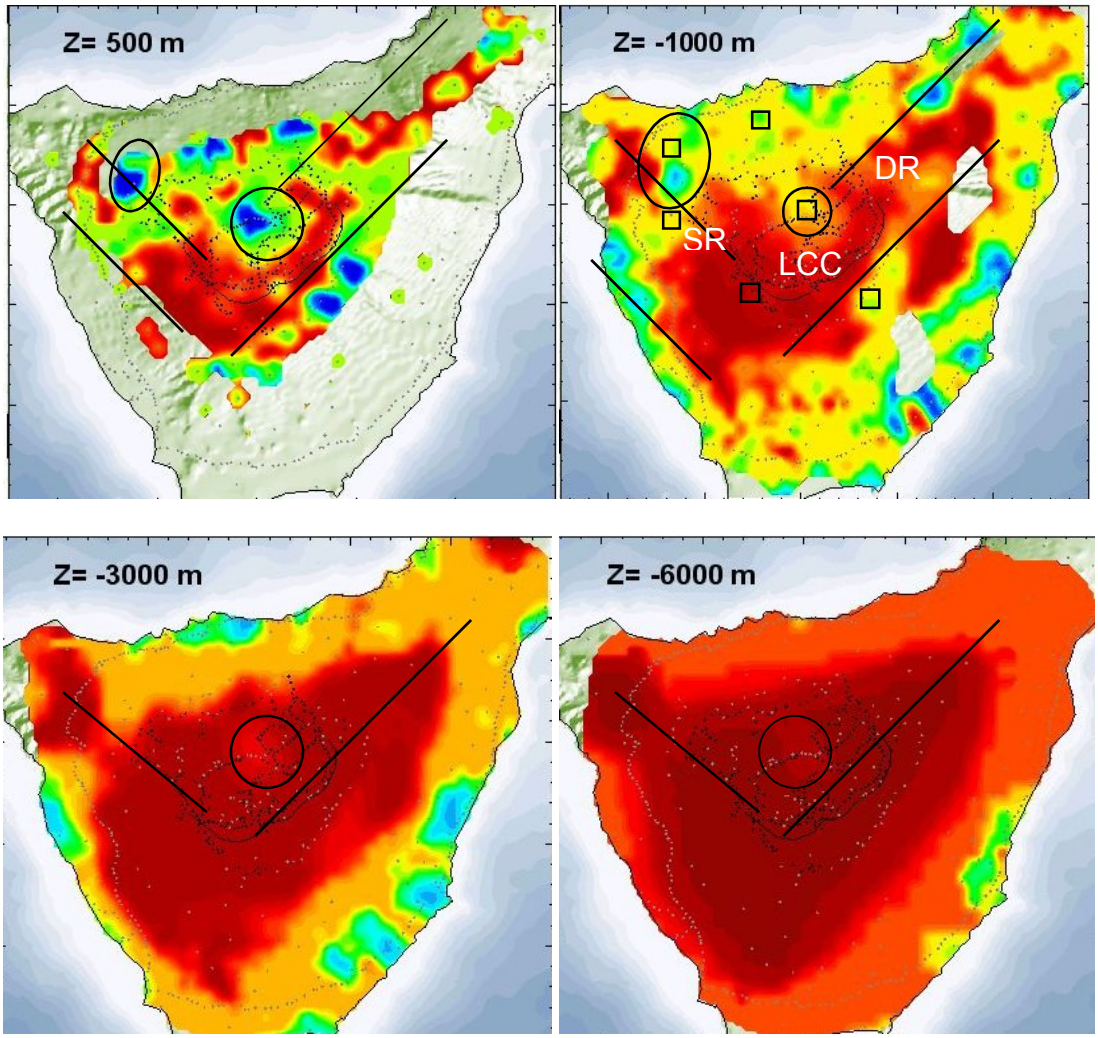

Figure 14